Hydrothermally altered shear zones: A new reservoir play for the expansion of deep geothermal exploration in crystalline settings

Alan Bischoff, Michael Heap, Perttu Mikkola, Jukka Kuva, Thierry Reuschlé, Ester Jolis, Jon Engström, Heini Reijonen, Tuomas Leskelä

Geothermics 118 (2024) 102895

Contents lists available at ScienceDirect

Geothermics

journal homepage: www.elsevier.com/locate/geothermics

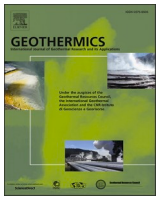

Hydrothermally altered shear zones: A new reservoir play for the expansion of deep geothermal exploration in crystalline settings

Alan Bischoff [a,*], Michael J. Heap [b,c], Perttu Mikkola [a], Jukka Kuva [a], Thierry Reuschlé [b], Ester M. Jolis [a], Jon Engström [a], Heini Reijonen [a], Tuomas Leskelä [a]

[a] Geological Survey of Finland (GTK), Vuorimiehentie 5, PO Box 96, Espoo 02151, Finland
[b] Institut Terre et Environnement de Strasbourg, UMR 7063, Université de Strasbourg, CNRS, 5 rue René Descartes, Cedex, Strasbourg F-67084, France
[c] Institut Universitaire de France (IUF), 1 rue Descartes, Paris Cedex 05, Paris 75231, France

ARTICLE INFO

Keywords:
Geothermal reservoirs
Shear zones
Hydrothermal alteration
Crystalline settings
Cataclasis
Fennoscandian Shield

ABSTRACT

Our study investigates the genesis of granitic reservoirs formed within a brittle shear zone in central Finland, evaluating their feasibility as deep geothermal targets. We employ a suite of laboratory-based experiments and cutting-edge analytical mineral techniques to determine the petrophysical and thermal properties of targeted granitic rocks, elucidating their formation processes. The most favorable reservoir properties were observed in granites affected by cataclasis and mineral dissolution, leading to a notable secondary porosity of ~20 %. Reservoir quality is largely controlled by the pore network morphology. Alongside fractures, interconnected moldic, sieve, and interparticle pores contribute to substantial permeability of ~5 × 10^{-14} m^2 (50mD), even under high confining pressures of 50MPa (~2km). A new geothermal play is here presented: brittle shear zones that have undergone high-temperature (~200–300 °C) hydrothermal alteration. These findings will significantly enhance our capacity to identify and exploit prolific permeable zones in deep crystalline settings globally, thereby making a substantial contribution to our ongoing transition to cleaner energy resources.

1. Introduction

The transition from fossil fuels to sustainable energy sources requires novel technologies that can meet large-scale commercial demands. Exploring deep geothermal resources in crystalline settings offers a promising solution for near-unlimited clean energy across multiple spheres of our society, including direct space heating, industrial applications, and electricity generation. However, geothermal exploration in deep crystalline settings presents unique challenges, particularly due to the typically low porosity and low permeability of crystalline rocks (Achtziger-Zupančič et al., 2017; Snowdon et al., 2021).

Faults and fractures are understood to play a substantial role in defining permeable zones that enable the movement of geothermal fluids within crystalline rocks, thereby facilitating efficient heat extraction from crystalline reservoirs (Gudmundsson et al., 2001; Genter et al., 2010; Vidal et al., 2017; Frey et al., 2022). Nevertheless, fractures constitute just a part of the void space in crystalline rocks. Besides fracturing, other equally important processes such as brecciation, cataclasis, and mineral dissolution significantly contribute to the formation of interconnected pores within crystalline reservoirs (Sausse and Genter, 2005; Staněk and Géraud, 2019; Stimac et al., 2019; Voutilainen et al., 2019; Duwiquet et al., 2021). Predicting the genetic processes, petrophysical characteristics, and pore connectivity of crystalline reservoirs remains a key obstacle in deep geothermal exploration.

Here we present a novel perspective on the formation of crystalline reservoirs, shedding light on the intricate interplay between brittle deformation and mineral alteration mechanisms that shape the pore network of granitic rocks. Our work does not address the challenges associated with the development of Hot Dry Rock (HDR) reservoirs, or the complex thermo-hydraulic-mechanical aspects of Enhanced Geothermal Systems (EGS), which have been extensively discussed in previous studies (e.g. Brown et al., 1999; Breede et al., 2013; Jolie et al., 2021; Kraal et al., 2021; Frey et al., 2022; Kukkonen et al., 2023). Instead, we focus on laying out critical geological processes that will enable the identification of novel opportunities for geothermal exploration in deep crystalline settings, particularly in challenging low-enthalpy areas where volcanic and rifting activity is absent. Furthermore, our study assesses the permeability variation of a suite of

* Corresponding author.
E-mail address: alan.bischoff@gtk.fi (A. Bischoff).

https://doi.org/10.1016/j.geothermics.2023.102895
Received 19 September 2023; Received in revised form 1 December 2023; Accepted 9 December 2023
Available online 16 January 2024

granitic reservoirs under increasing confining pressure, providing valuable insights into their suitability as deep geothermal targets. Given the geographical constraints of conventional high-temperature geothermal systems, identifying unconventional geothermal prospects, such as deep hydrothermally-enhanced fracture zones in crystalline cratons, will broaden our exploration targets as technology enables their development. Ultimately, our findings will help to expand geothermal energy exploration and production in crystalline settings typically regarded as risky by the geothermal industry, contributing significantly to our ongoing transition to cleaner and more reliable energy resources.

2. Geological setting

Our study area lies within the Karelia Province, central Finland (Fig. 1), a collage of Precambrian accretionary terranes and remnants of oceanic crust that constitute part of the Fennoscandian Shield. During the Archean, mantle segregation and continental growth gave rise to ~2.80Ga TTG (tonalite–trondhjemite–granodiorite) gneisses that were migmatized and intruded by leucogranites at ~2.70Ga (Lauri et al., 2006; Hölttä et al., 2021). Rifting of the Archean crust began at 2.44Ga, resulting in voluminous mafic-ultramafic magmatism along with few A-type granitic intrusions and episodic emplacement of dike swarms until 1.98Ga (Vuollo and Huhma, 2005; Lauri et al., 2012; Kärenlampi et al., 2019). The onset of the Svecofennian orogeny at ~1.91Ga initiated a compressional tectonic phase that resulted in multiple continental collisions and the development of large-scale shear zones that remained active until at least 1.79Ga (Kontinen et al., 2013; Nironen, 2017). This event induced metasomatic alterations on the Karelian crust, predominantly within narrow shear zones (Pajunen and Poutiainen, 1999), and more widespread rehydration reactions that affect both the Archean and Paleoproterozoic rocks (Hölttä and Heilimo, 2017). At the end of the Paleoproterozoic, the Karelia Province became a relatively stable craton, experiencing only limited subsequent deformation events related to orogens in western Fennoscandia, localized intraplate magmatism, and glacial-isostatic adjustments (Kohonen and Rämö, 2005; Green et al., 2022).

3. Drill core overview

Our samples originate from the deeper 1250–1722m interval of the Koillismaa Deep Drillhole, commissioned by the Geological Survey of Finland in 2021 and drilled near the locality of Kuusamo, central Finland (Fig. 1). This area has been a subject of scientific and geoeconomic research since the 1970s, primarily driven by the existence of the 2.45Ga Koillismaa and Näränkävaara mafic-ultramafic layered intrusions and their associated Cu-Ni-PGE, V-Ti-Fe mineralizations. An unresolved question centered on the origin of the 60km-long Bouguer gravity anomaly linking these intrusive complexes. To investigate, GTK launched the Koillismaa Deep Hole project in 2020, initially targeting a 3km deep borehole capable of sampling this geophysical anomaly. However, drilling encountered substantial challenges due to highly fractured rocks within a fault zone. Consequently, after four months of drilling, the borehole only reached a depth of 1724.7m. An attempt to sidetrack it faced similar issues and the second drilling was halted at a depth of 1594.9m.

The uppermost 658m of this borehole penetrated TTG gneisses that are intruded by leucogranites and diabase dikes of varying widths. The central section (658–1410m) consists of homogeneous granites and quartz diorites. Below 1410m, granites are interfingering and locally intermingling with mafic-ultramafic rocks that correlate with the layered intrusions of the Tornio-Näränkävaara belt (Lauri et al., 2006). The gneisses were dated as Archean (2.9–2.8Ga), while the granites and diabase dikes crystallized at ~2.44Ga (Anttilainen, 2023). Geochemically, the granites exhibit an anorogenic A-type signature, whereas the diabase dikes show calc-alkaline composition (Anttilainen, 2023). Collectively, structural, petrological, geochronological, and geochemical observations strongly indicate that Proterozoic felsic and mafic melts were coeval, both belonging to the ~2.44Ga bimodal magmatism related to the rifting of the Archean crust.

The fractured and altered ultramafic rocks proved to be too fragile, preventing us from obtaining suitable drill cores for petrophysical studies. Additionally, presenting the full range of rocks and their variations would make this paper overly dense. Thus, prioritizing clarity, we have chosen to solely work with the anorogenic granites, while only limited data from the ultramafic rocks are presented in Appendix 1.

4. Reservoir characterization

We classified the granites into four groups based on their reservoir properties: (1) massive, (2) fractured, (3) brecciated, and (4) altered granites. The fractured granites were subdivided into three sub-groups, based on the morphology of their fractures: (2a) open regular, (2b) open irregular, and (2c) closed disconnected fractures (Fig. 2).

The massive granites represent the original rock formed through the crystallization of felsic magma, with its initial structure and composition remaining largely unaffected by post-emplacement processes. The main minerals comprise quartz, plagioclase (albite and oligoclase), and K-feldspar. Mafic phases account for ~10 % of the rock and include biotite and minor occurrences of hornblende and pyroxene that are occasionally partially replaced by chlorite. Accessory minerals such as titanite, apatite, allanite, and zircon are also present (Fig. 3a and b; Appendix 1).

Post-emplacement processes such as brittle deformation and mineral alteration play a crucial role in modifying the structure and composition of massive granites (Sausse and Genter, 2005; Duwiquet et al., 2021). We observed that these processes lead to the development of characteristic pore networks, each having diverse impacts on the storage capacity (porosity) and fluid flow properties (permeability) of granitic reservoirs (Table 1). The encountered variations of the massive granite are described in detail in the subsequent section.

4.1. Pore network and its effects on reservoir quality

Fractured granites display regular, irregular, and disconnected cracks that are associated with minor occurrences of moldic, intracrystal, and microfracture pores (Videos Koi-03c, Koi-05b, Koi-07b, Koi-08b, and Koi-09b in Supplementary Data). Open regular fractures are smooth and have parallel walls, forming a tabular geometry with a maximum aperture of 650 μm (Figs. 2, 4a, and 5). In contrast, open irregular fractures have rough walls and a larger maximum aperture of 1230 μm (Figs. 4b and g, and 5), whereas closed disconnected fractures typically appear as a series of thin (<80 μm) intersecting cracks with limited lateral extension (Fig. 4c). The morphology of the fractures is understood to result from the interplay between rheological properties of the host material (e.g. microstructure, mineralogy, presence of pre-existing structures and textures; Atkinson, 1984; Cartwright-Taylor et al., 2020) and the environmental conditions where the cracks occur (e.g. pressure, temperature, presence of water; Rizzo et al., 2018; McBeck et al., 2021). Additionally, we note that subsequent mineral alteration along fracture walls leads to the formation of irregular fractures with increased aperture (Fig. 4b, e, and g), as also reported by Sausse and Genter (2005).

Irrespective of their formation process, we observe that fracture morphology significantly influences the reservoir properties of the studied rocks. Closed disconnected fractures do not enhance reservoir quality substantially; their petrophysical behavior aligns with that of massive granites (Fig. 6). Likewise, fracturing alone typically adds little porosity, up to 4 % of the total rock mass for individual samples (Table 1). Conversely, the influence of pore morphology on permeability is most pronounced, particularly as confining pressure is increased. At a low confining pressure of ~1MPa, open regular fractures have a high permeability of nearly 10^{-12} m^2, which is drastically reduced to 10^{-20} m^2 at 50MPa (~2km deep in crystalline settings). By contrast, increasing

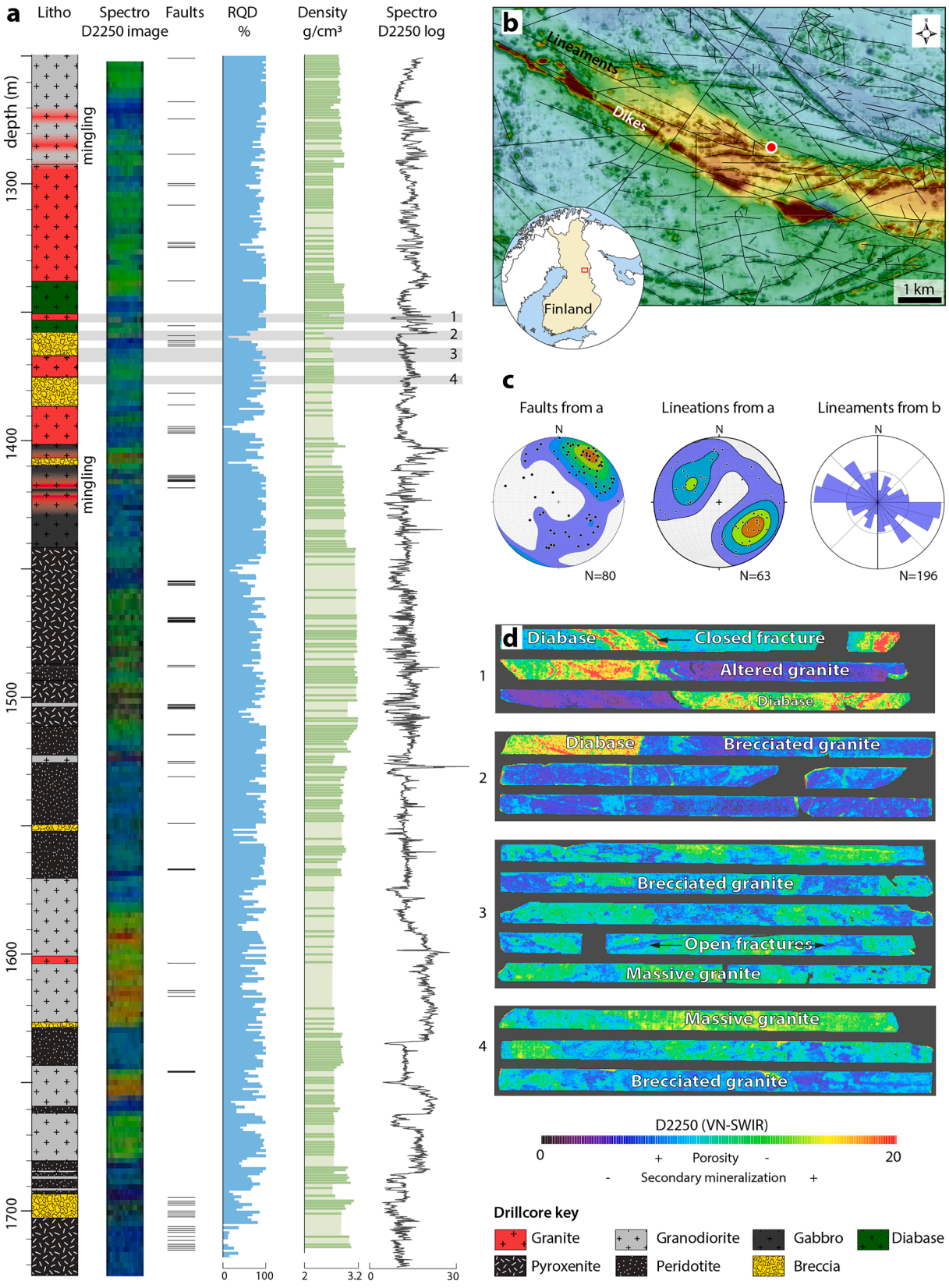

Fig. 1. (a) Composite borehole data displaying the lithology, D2250 scalar based on hyperspectral data, location of faults, RQD, and rock density of the studied interval. The darker green color on the density log corresponds to the location of the analyzed samples. (b) Regional lineament interpretation overprinted on the aeromagnetic map of the area. The red dot marks the drillhole location. (c) Stereonets show the pole of planes of faults and lineations identified in the Koillismaa borehole while the Rose Diagram displays the trend of lineaments from the area. (d) Detailed plot of hyperspectral D2250 scalar of key intervals. For the granitic rocks, hot colors highlight the presence of secondary minerals, closed fractures, and massive rocks while the cold colors show textures such as rock fragmentation, open fractures, and pores.

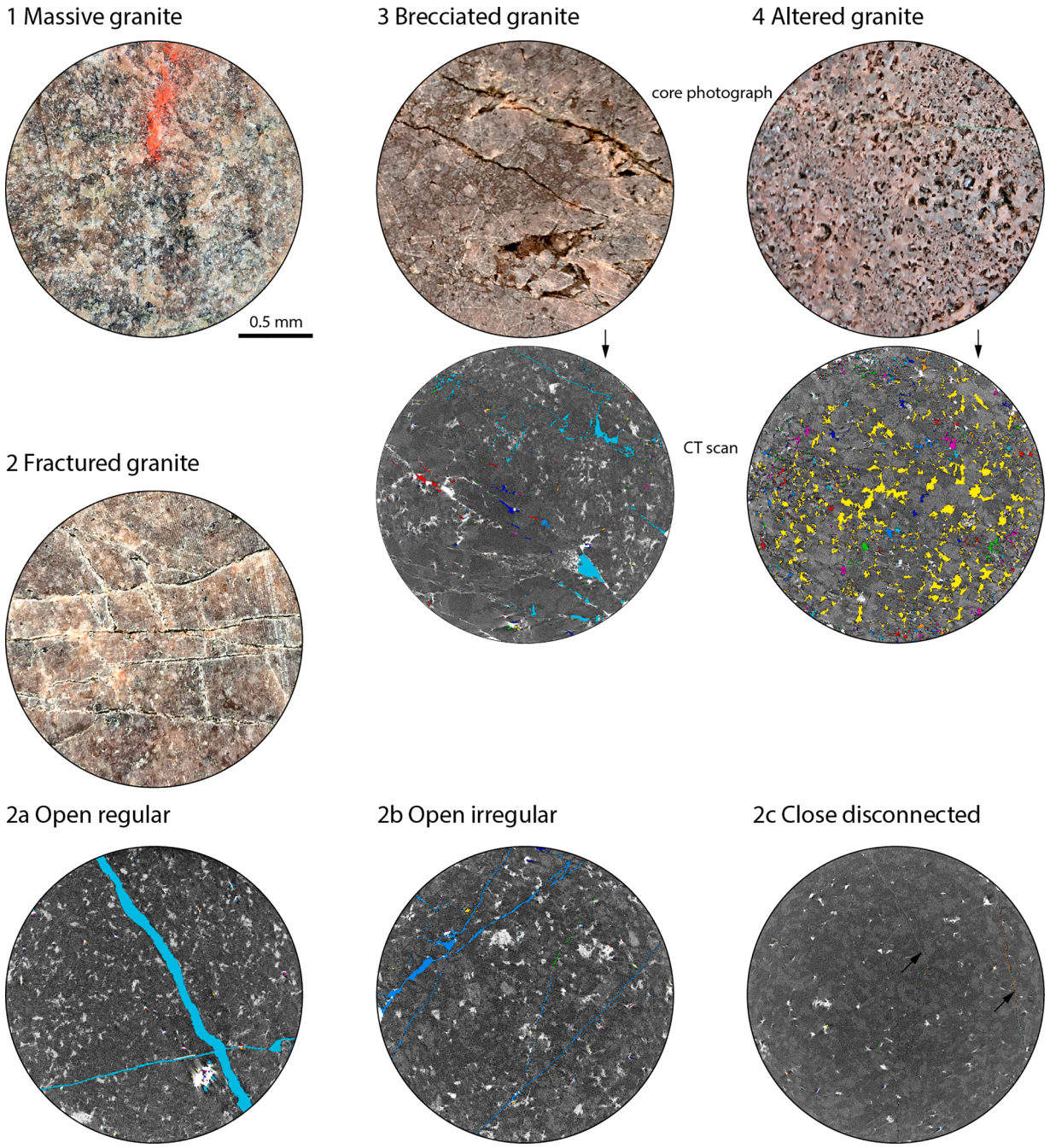

Fig. 2. Pore network classification of the main granitic rock types within our dataset. Granites were classified into (1) massive, (2) fractured, (3) brecciated, and (4) altered. Fractured granites were further divided into (2a) open regular, (2b) open irregular, and (2c) closed disconnected. CT scan pore segmentation is highlighted in colors while the mineral density is displayed in grey shades.

confining pressure from 1 to 50MPa only reduces the permeability of open irregular fractures from 10^{-14} to 10^{-16} m^2 (Fig. 6f). We conclude that poorly mated fracture walls and disparate surfaces prevent fractures from closing, even under high confining pressures, thus enabling more efficient fluid migration at depth. While the elevated tortuosity of irregular fractures may degrade reservoir quality (Sausse and Genter, 2005; McBeck et al., 2021), the enlargement of fracture walls can increase permeability and expand the reservoir volume, critical factors that enhance the reservoir performance of geothermal targets (Ledésert et al., 2009; Wyering et al., 2014; Heap and Kennedy, 2016).

Brecciated granites have distinct characteristics, including intense particle fragmentation, and significant grain size reduction. This often leads to the creation of a fine-grained (<1mm) rock composed of a matrix resembling the products of glass devitrification (Figs. 1, 4, and 5; video Koi-02c in Supplementary Data), typical textures of brittle fault rocks such as cataclasites, ultracataclasites, and pseudotachylites (e.g. Schmid and Handy, 1991; Faulkner et al., 2008; Fossen et al., 2017). Pore types within the brecciated granites include polyhedral fractures, sieve, interparticle voids, microfractures (<0.5mm), and large (~1cm) vugs, which combined account for moderate porosity of up to 7 % and mean pore size of 180 μm (Table 1; Figs. 2 and 5). In detail, interparticle pores exhibit undulating surfaces with pore sizes usually <100 μm (Fig. 5). These pores are interpreted to result from crushing, grinding, and particle rotation at brittle shear zones (Fig. 4f). Additionally, fractures are widespread in the brecciated granites and typically occur at the crystal boundaries and parallel to the crystal cleavage (Fig. 5h). We also

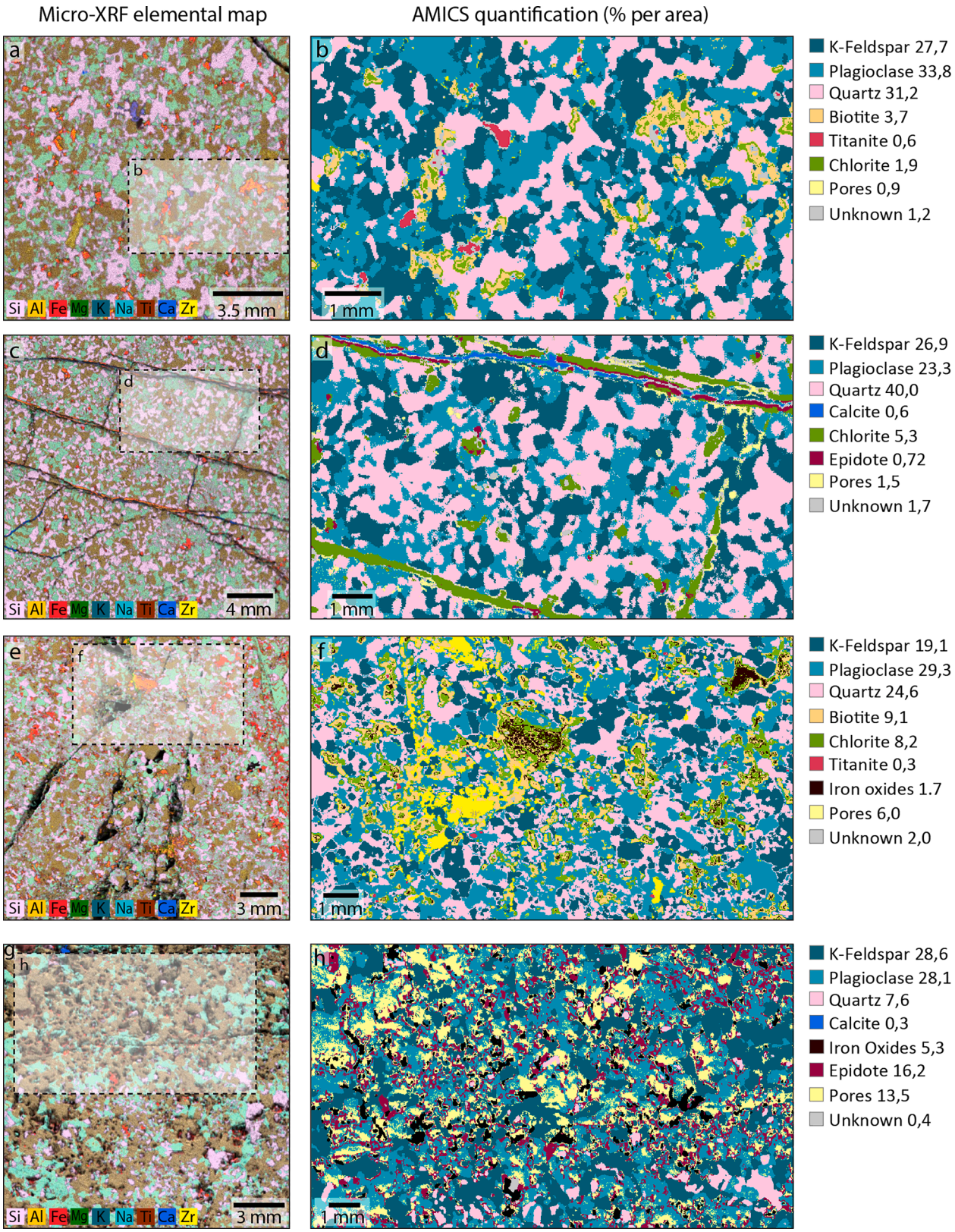

Fig. 3. Micro-XRF results showing the chemistry, mineral composition, and pore quantification of selected representative samples. (a and b) Massive granite. (c and d) Fractured granite with closed and disconnected fractures. (e and f) Brecciated granite. (g and h) Altered granite.

observe that the fine-grained cataclastic matrix is often associated with sieve pores, a process commonly observed in igneous rocks that have experienced alteration, glass devitrification, and material remobilization (e.g. Sruoga and Rubinstein, 2007; Bischoff et al., 2021). Contrasting to fractured granites, brecciated granites initially exhibit lower permeability at low confining pressure, but when subjected to higher confining pressures, their permeability has a less pronounced decrease (1.91×10^{-15} to 1.79×10^{-16} m^2) (Fig. 6f). As for irregular

Table 1
Facies, pore types, petrophysical, and thermal properties of the diverse granitoids investigated in this study.

Sample	Depth	Facies	Pore types	Density (g/cm^{-3})	Effective porosity (%)	Pore connectivity (% CT scan)	Aperture mean and max (μm)	Permeability (m^2) at 1 MPa	Permeability (m^2) at 50 MPa	Thermal conductivity wet (W/mK)	Thermal conductivity dry (W/mK)	P-wave velocity (km/s)
Koi-01a	1351.10	Altered qz-monzonite	Moldic, sieve, intracrystal, and microfractures	2.40	17.19					2.03	1.83	4.887
Koi-01b	1351.20			2.24	16.90	74.5	153; 734	5.49E-14	3.97E-14		1.75	4.261
Koi-01c	1351.13			2.32	6.85							3.476
Koi-02a	1364.10	Brecciated granite	Polyhedral fractures, interparticle, sieve, vug, and microfractures	2.58	3.25					2.97	2.70	5.403
Koi-02b	1364.13			2.58	3.06					2.74	2.37	5.684
Koi-02c	1364.20			2.56	6.88	74.6	178; 1199	1.91E-15	1.79E-16		2.81	5.221
Koi-03a	1385.25	Fractured granite	Open irregular fractures, minor moldic and intracrystal	2.60	1.28					1.78	1.30	5.881
Koi-03b	1385.28			2.61	1.15					1.69	1.62	5.633
Koi-03c	1385.32			2.60	4.10	81	202; 1232	2.84E-14	1.84E-16		3.23	5.876
Koi-04	1388.88	Massive granite	Minor intercrystal and microfractures	2.65	0.43					3.24	3.14	5.653
Koi-05a	1421.95	Fractured granite	Closed disconnected microfractures	2.59	1.28					3.19	3.39	5.643
Koi-05b	1421.98			2.59	3.59	30.3	82; 386	9.45E-18	6.94E-20		3.27	5.656
Koi-07a	1575.90	Fractured granite	Closed disconnected microfractures	2.66	0.68					2.95	2.97	5.603
Koi-07b	1575.93		Open regular fractures		1.70	95.8	256; 647	9.54E-13	1.76E-20			
Koi-08a	1629.20	Fractured granodiorite	Open irregular fractures, minor moldic and intracrystal	2.64	1.72					1.53	1.05	5.503
Koi-08b	1629.23		Closed disconnected microfractures	2.65	1.76	32.4					2.90	5.868
Koi-09a	1664.60	Fractured granodiorite	Open regular fractures	2.64	1.26					1.54	1.52	5.481
Koi-09b	1664.63			2.65	3.84	32	53; 152	8.10E-13	3.31E-18		2.72	4.429
Koi-10a	1694.35	Brecciated granodiorite	Polyhedral fractures, interparticle, sieve, vug, and microfractures	2.69	3.86					1.93	1.76	
Koi-10b	1694.38	Altered granodiorite	Moldic, sieve, intracrystal, and microfractures	2.57	9.14							1.773

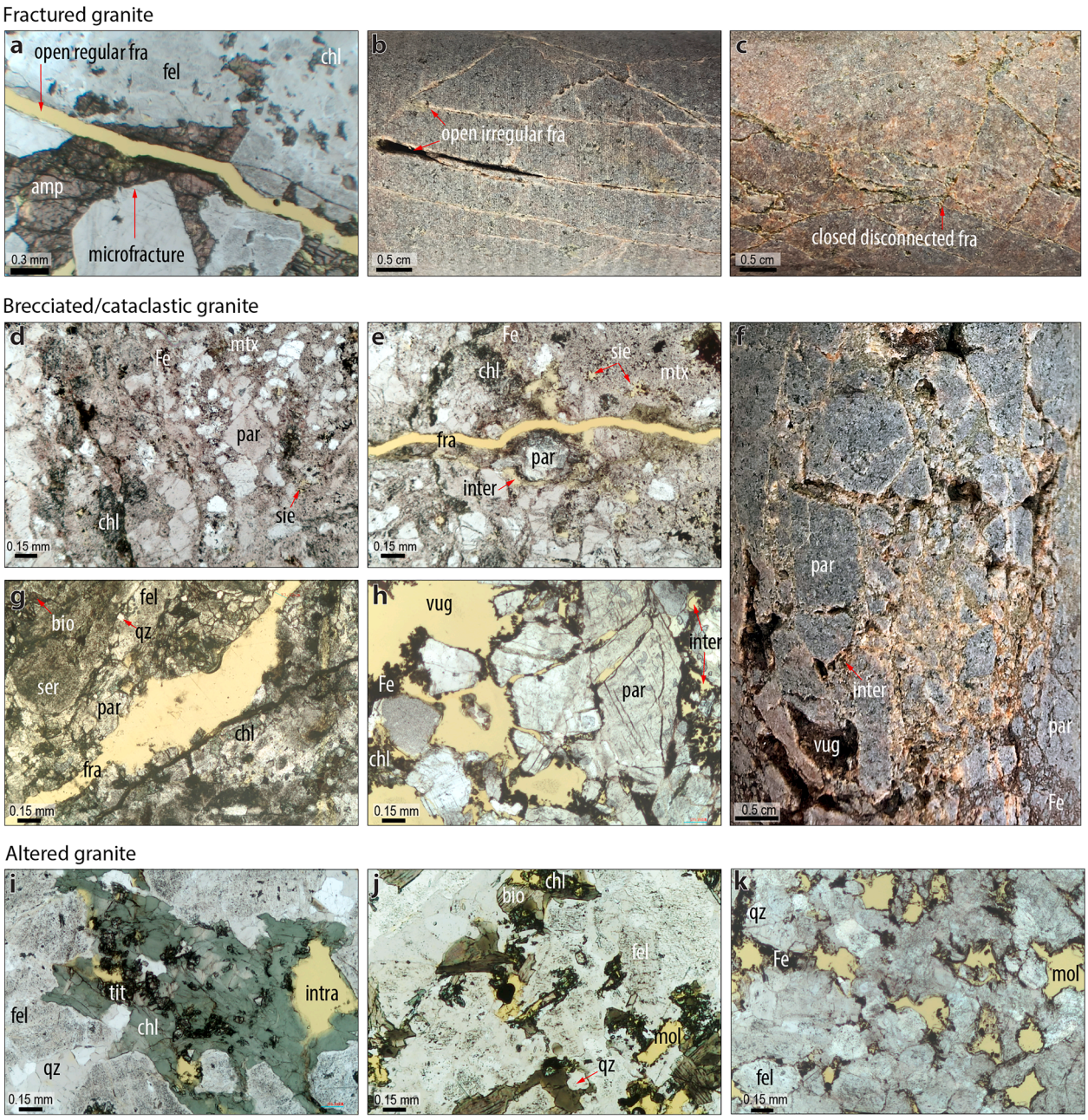

Fig. 4. Drilling core photographs (b, c, and f) and thin-section images in plain polarized light (a, d, e, g, h, i, j, k) showing the minerals, textures, structures, and pore types of the granitic reservoirs identified in this study. Abbreviations are: tit (titanite), fel (feldspar), qz (quartz), amp (amphibole), bio (biotite), chl (chlorite), epi (epidote), ser (sericite), Fe (iron oxides, including magnetite, hematite, and ilmenite), py (pyrite), par (particles, referring to cataclastic grains >1mm in size), mtx (matrix, referring to cataclastic grains <1mm), fra (fracture pore), inter (interparticle pore), intra (intracrystal pore), sie (sieve pore), vug (vug pore), and mol (moldic pore). Rock porosity is highlighted in yellow.

fractures, we conclude that the intricate pore network of brecciated granites enables fluid movement to be moderated even at depths of nearly 2km.

From our rock subset, altered granites possess the most favorable petrophysical properties to form deep geothermal reservoirs (Fig. 6f; video Koi-01b in Supplementary Data). These rocks display moldic, sieve, intracrystal, and microfracture pores that account for up to 17 % porosity (Table 1), an unusually high porosity for plutonic rocks. We observe that these pores formed by the alteration and leaching of biotite (mainly), amphibole, pyroxene, and plagioclase (Fig. 3). Mafic phases are partially or totally replaced by chlorite and epidote while sericite and epidote substitute plagioclase (Fig. 4i, j, l, and m). This alteration paragenesis matches the propylitic type, a phenomenon that results from the interaction of hot (~200–300 °C) hydrothermal fluids with igneous rocks (e.g. Nishimoto and Yoshida, 2010; Sanchez-Alfaro et al., 2016; Weydt et al., 2022). Moldic pore sizes are up to 2000 μm while intracrystal pores have a maximum pore size of 730 μm, both exhibiting anhedral morphology with undulating and polyhedral surfaces, indicating their conformity to the original shape of biotites and amphiboles (Fig. 5). Sieve pores are commonly associated with plagioclase sericitization, forming small (<100 μm) and dispersed voids. Additionally, microfractures occur at crystal boundaries and cleavages. The effects of confining pressure (i.e. simulated burial depth) on the porosity and permeability of altered granites are minimal (Fig. 6f; Appendix 1): from 1 to 50MPa, we observe little porosity change (16.90 to 15.70 %, corresponding to 1.2 % decrease) and small permeability reduction (5.49 ×

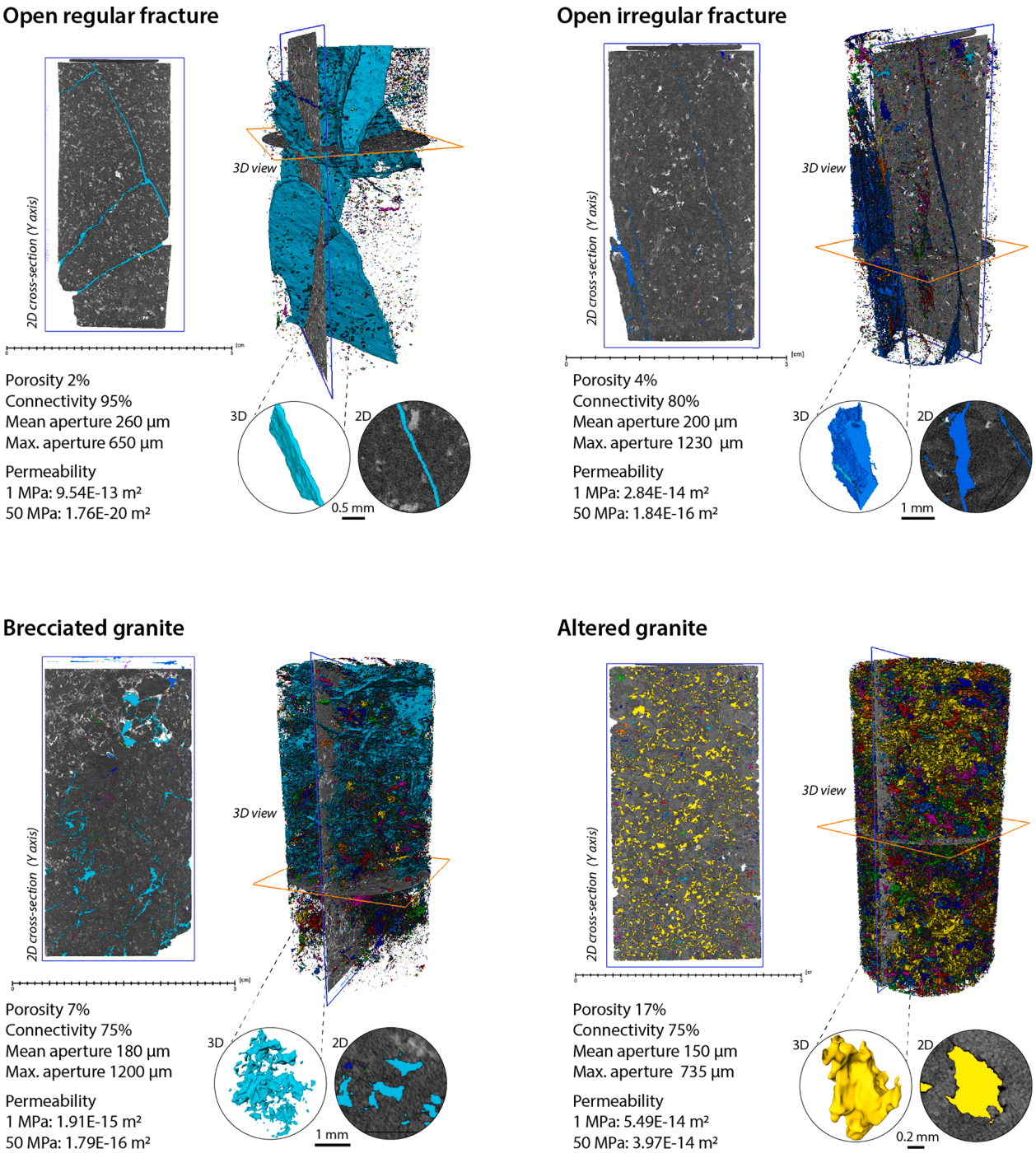

Fig. 5. CT scan images highlighting the pore morphology and connectivity of four types of granitic reservoirs found within a hydrothermally altered shear zone. Low-density regions that correspond to void volumes were colored to facilitate the visualization of the pores. Porosity values are from gas pycnometer measurements whereas the permeability values are from steady-state and pulse decay measurements at increasing confining pressures (Table 1). Pores of the same color are connected at a limit of 11 µm resolution (connectivity label displayed as a percentual value). CT scan videos are provided as part of the supplementary material.

10^{-14} to 3.97 × 10^{-14} m^2, equivalent to 15.4mD reduction). Similar results have been documented in a recent publication that describes the reservoir properties of fault-related hydrothermally altered granites in the Cornwall geothermal prospect, UK (Inskip et al., 2023). We conclude that the altered granites can sustain high permeability at depth because, compared to fractured and brecciated granites, the moldic and intra-crystal pores within the altered granite are not compliant and, as a result, do not close when subject to confining pressures. We highlight that the inelastic closure of these pores, which could promote reductions to permeability, would likely require several hundreds of MPa.

4.2. Porosity reduction through secondary mineralization

Locally, secondary mineralization of chlorite, epidote, and iron oxides accounts for substantial porosity reduction. These precipitation products are often sourced from the dissolution of iron-bearing mafic minerals such as biotite and pyroxene when in contact with hydrothermal fluids (Nishimoto and Yoshida, 2010; Hampl et al., 2022). Particularly, interparticle pores and fractures of brecciated granites are partially mineralized by iron oxides (hematite, ilmenite, and magnetite), comprising nearly 10 % of the total rock composition (Figs. 3c and 4f).

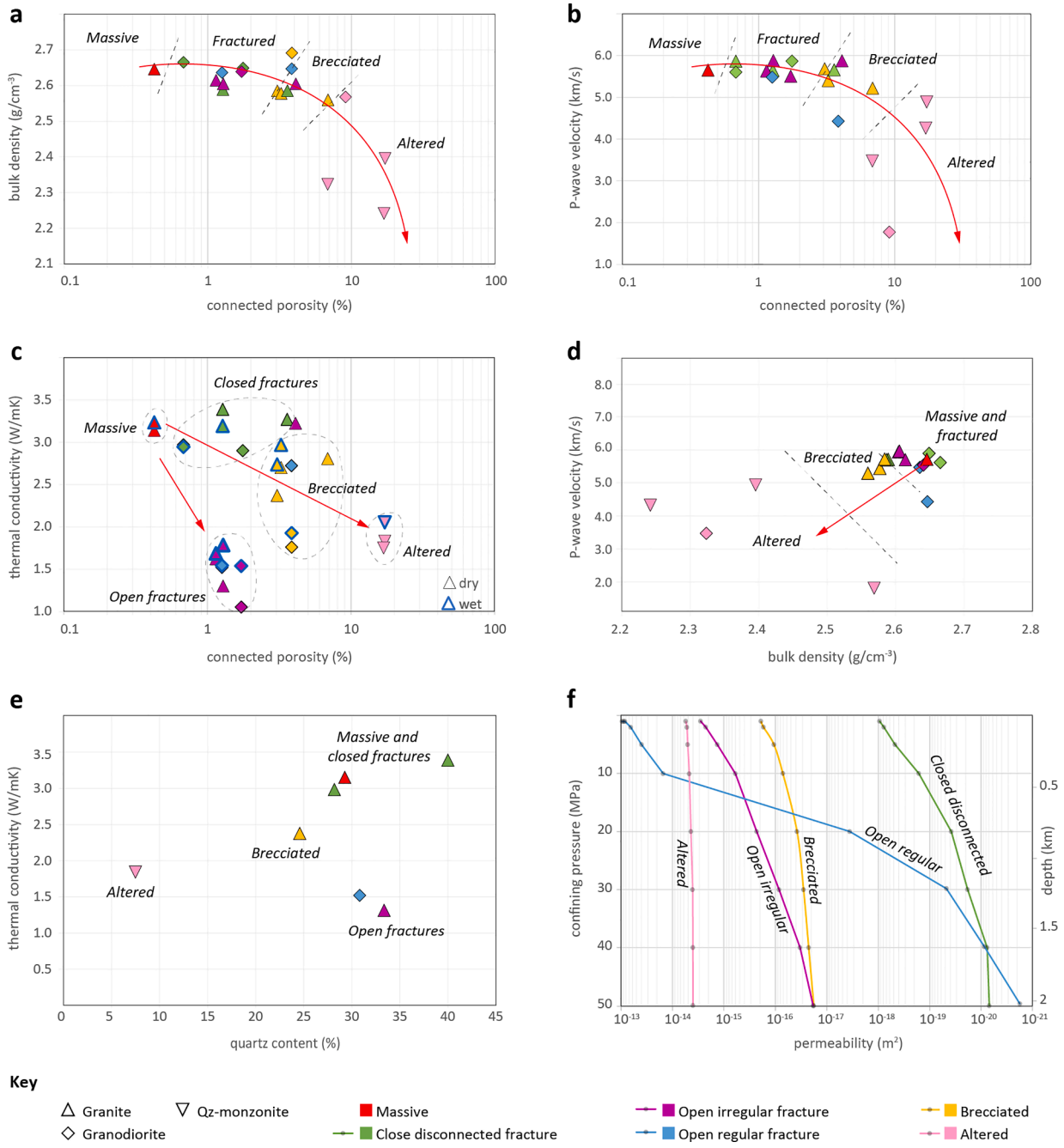

Fig. 6. Petrophysical and thermal data of the granitic rocks investigated in our study. The observed heterogeneity of these rocks is mainly controlled by their distinctive pore network, which in turn, is determined by brittle deformation (fracturing and brecciations) and mineral alteration processes. Depths estimation in (f) considers a crystalline setting in which the lithostatic load is 2.6kg/cm^3.

Similarly, epidote veins typically crosscut the altered granites (Fig. 3d), in addition to iron oxides that often precipitate in the walls of irregular fractures and moldic pores (Fig. 4e and h). Combined, these minerals account for over 20 % of the composition of altered granites, indicating substantial porosity reduction due to secondary mineralization. Conversely, calcite veins are less common, accounting only for <1 % of the analyzed rocks (Fig. 3).

5. Controls on petrophysical and thermal heterogeneity

After magma crystalization, post-emplacement processes of fracturing, brecciation, mineral alteration, and secondary mineralization become pivotal factors shaping the petrophysical and thermal properties of the studied granites. Overall, the bulk density and the P-wave velocity of our samples reduce as the porosity increases (Fig. 6a and b; Table 1), as commonly observed for most rock types (e.g. Nasseri et al., 2007; Griffiths et al., 2017; Kushnir et al., 2018). Relative to the rocks within our dataset, massive granites typically have the lowest porosity (<1 %), high density (2.65g/cm^3), and high P-wave velocity (5.65km/s). These attributes align with typical low permeability (<10^{-16} m^2) granitic rocks, which in their natural state are poor geothermal prospects due to their limited fluid and thermal flow yields (Meredith et al., 2012; Jolie et al., 2021; Piipponen et al., 2022). Next, fractured granites exhibit relatively low porosity (up to 4 %), high bulk density (ranging from 2.59 to 2.66g/cm^3), and the highest P-wave velocity values (between 5.48 and 5.88km/s). An exception is observed in the case of sample Koi-09b,

which has a lower P-wave velocity value of 4.43km/s (Table 1). This anomaly can be attributed to the presence of a large open fracture intersecting the sample (Video Koi-09b in Supplementary Data), which likely hinders P-wave propagation.

In contrast to massive granites, the brecciated granites exhibit relatively higher porosity (from 3 to 7 %), lower bulk density (between 2.56 and 2.58g/cm^3), and lower P-wave velocities of 5.22 to 5.68km/s (Fig. 6). Among the various rock types, the altered granites have the most pronounced petrophysical heterogeneity (Table 1; Figs. 5 and 6). These rocks typically display substantially high porosity (7–17 %) and, as a result, have the lowest bulk density (ranging from 2.24 to 2.57g/cm^3) and the lowest P-wave velocity (between 1.77 and 4.88km/s). The reduced P-wave velocity of the altered granites may play a pivotal role in enhancing their geophysical prospectivity using seismic reflection methods.

As observed in the analysis of fluid flow properties from different fractured granites (as presented in Section 4.1), it becomes evident that pore morphology also has a significant impact on thermal properties (Fig. 6c). Granites displaying closed disconnected fractures demonstrate thermal conductivity values comparable to those of massive granites, with values ranging from 2.90 to 3.39W/mK for both wet and dry samples. Conversely, thermal conductivity significantly decreases in brecciated and altered granites (from 1.56 to 2.97W/mK), while the most pronounced reduction is observed in granites with open fractures, where values range from 1.05 to 1.78W/mK for both wet and dry samples (Table 1). Exceptions are noted in the cases of samples Koi-03c and Koi-09b, both of which have open fractures but exhibit relatively high thermal conductivity values of 3.23 and 2.72W/mK, respectively. These anomalies may be attributed to the natural heterogeneities of the samples.

Additionally, we observed a consistent increase in thermal conductivity from dry to wet samples, a phenomenon commonly reported in the literature (e.g. Clauser and Huenges, 1995; Heap et al., 2020). However, contrary to the conventional expectation that increasing porosity should lead to lower thermal conductivity (e.g. Kushnir et al., 2018; Heap et al., 2020), our dataset reveals a more intricate relationship. Particularly, granites characterized by the presence of open fractures, despite having relatively low porosity, exhibit much lower thermal conductivity values compared to altered granites that possess significantly higher porosity (Fig. 6c). We attribute the significant decrease in thermal conductivity of granites with open fractures to the insulating effect created by the cracks, which hinders heat transfer. In the case of altered granites, the more unbroken contact between crystals still enables heat conductivity, even when the porosity is higher (Fig. 4). We also evaluate the influence of mineral composition on thermal conductivity, particularly quartz content, which has a very high thermal conductivity of ~6W/mK (Clauser and Huenges, 1995). However, our findings indicate that this factor has a much less pronounced effect on our sample set of granites, granodiorites, and quartz-monzonites (as shown in Fig. 6e) when compared to the substantial impacts of pore-network morphology (Fig. 6c).

It is important to note that these results stem from a limited dataset. Thus, their broader implications can only be fully understood as more comprehensive petrophysical datasets involving altered and fractured granites become widely available from diverse geological settings.

6. Discussion

6.1. Origin of the crystalline reservoirs

Our hypothesis concerning the genesis of the studied granitic reservoirs is that far-field stress at the foreland of the Svecofennian orogenic front initiated brittle shearing and faulting, which in turn, facilitated the migration of hot fluids and subsequent hydrothermal alteration. This interpretation is based on our borehole dataset, which reveals that strike-slip faults associated with secondary porosity align with the northwest-southeast trend of nearby shear zones activated during the Svecofennian orogeny (Fig. 1b and c). Shear zones located closer to collision fronts underwent peak metamorphism of around 600 °C and 5kbar at 1.85Ga, whereas our study area was significantly less affected by the Svecofennian overprint (Pajunen and Poutiainen, 1999; Nironen, 2017). This is evident by the progressive westward metamorphic gradient affecting Precambrian supracrustal rocks in the Karelian Province. Eastern supracrustal rocks near the study area experienced lower greenschist facies, while the western Karelia was metamorphosed to upper amphibolite conditions (Laajoki, 2005). In addition, K-Ar dating of biotites and hornblendes yield Neoarchean ages in our study area, indicating that temperatures have remained below 300 °C since the Archean. In most other parts of the Karelia Province, these ages have been reset to 1.9–1.8Ga due to the burial of the Karelian crust under Svecofennian nappes and subsequent heating to temperatures exceeding 500 °C (Kontinen et al., 1992). Temperatures below 300 °C would still allow propylitic alteration at the formation of the granitic reservoirs, as this alteration type has been interpreted to take place under temperatures of approximately 200–300 °C (e.g. Nishimoto and Yoshida, 2010; Weydt et al., 2022).

Alternatively, the genesis of the crystalline reservoirs might be tentatively attributed to events other than the Svecofennian orogeny. We have observed propylitic alteration occurring at the contact of Paleoproterozoic diabase intrusions, implying that diking may play a role in the formation of crystalline reservoirs. The location of Paleoproterozoic mafic-ultramafic intrusions beneath coeval volcanic units suggests magma emplacement at relatively shallow crustal levels (Lauri et al., 2006), thus allowing for brittle deformation and the development of secondary porosity shortly after magma crystallization and cooling at 2.44Ga. However, the contacts of dike intrusions are typically associated with strike-slip faults (Fig. 1), indicating a tectonic contact rather than an igneous intrusive boundary. Based on this observation, is more likely that dike contacts served as inherited pathways for fluid migration rather than be the primary source of fluids inducing propylitic alteration. Furthermore, any porosity predating the Svecofennian orogeny should exhibit overprinting effects, including burial compaction textures such as pore collapse, syntaxial mineral overgrowth near pore walls, and pressure solution mineralization at grain boundaries (e.g. Mørk and Moen, 2007; Bossennec et al., 2021). This is especially relevant given that the Karelia Province was buried to depths of 10–15km during the late Paleoproterozoic (Kontinen et al., 1992). On the contrary, we observe that moldic pores preserve the original shapes of mafic minerals (Figs. 3 and 4) indicating mild burial effects, supporting the hypothesis that the porosity of our rock samples formed after the Svecofennian orogeny peak at 1.85Ga. After the Svecofennian orogeny, the exhumation of the Fenoscandian bedrock appears to have been relatively rapid, as indicated by the emplacement of anorogenic rapakive granites in Southern Finland at depths of approximately 5km around 1.65Ga (Rämö and Haapala, 2005).

Far-field deformation and foreland sedimentation linked to the Gothian (1.75–1.50Ga), Sveconorwegian (1140–960Ma), and Caledonian (490–390Ma) orogens in western Fennoscandia, localized Devonian intraplate intrusions, and Neogene glacial-isostatic adjustments are additional potential contributors to the genesis of the granitic reservoirs here studied. However, the relatively high temperature necessary for propylitic alteration contradicts its formation as being younger than the late Paleoproterozoic, as no thermal events of comparable magnitude have been recorded in the Karelia Province since the cessation of the Svecofennian orogeny (Kohonen and Rämö, 2005; Green et al., 2022). For example, by the end of the Silurian, a significant portion of present-day Finland was covered by a nearly 1.5km thick Neoproterozoic to Paleozoic sedimentary pile, which was later removed by erosion and exhumation of the Precambrian basement. Apatite fission track analysis indicates that the sedimentary burial across eastern Sweden induced maximum temperatures of 90 ± 15 °C during the Late Silurian to Early Devonian (Huigen and Andriessen, 2004). In a

conservative scenario where the sedimentary burial reached temperatures of 100 °C in our studied area, along with an additional 1.5km of crystalline rock cover (matching the present depth of the granitic reservoirs at the Koillismaa borehole), an extraordinarily high geothermal gradient of 66 °C/km would be necessary to initiate propylitic alteration—a condition that seems highly unrealistic. Relative to present-day eastern Sweden, the Karelian Province was located away from the western Fennoscandian collision fronts, and consequently, the study area has experienced progressively weaker paleo-thermal effects (Samuelsson and Middleton, 1998; Green et al., 2022). Thus, neither western orogens younger than the Paleoproterozoic nor the burial of the Karelian Province under Paleozoic sedimentary strata can properly explain the genesis of the crystalline reservoirs described here. This strengthens the argument in favor of the late stages of the Svecofennian orogen as the likely cause for the formation of the granitic reservoirs. Determining the ages of faults intercepted by the Koillismaa drillhole will provide additional details into the origin of these outstanding crystalline reservoirs.

6.2. Hydrothermally altered brittle shear zones as deep geothermal reservoirs

Altered and unaltered brittle shear zones have been previously exploited for geothermal energy, mainly in active tectonic and volcanic settings such as the Upper Rhine Graben in France (Ledésert et al., 2009), the Great Basin Region in the western USA (Faulds et al., 2011), and in the Northern Apennines, central Italy (Brogi et al., 2003). To a much lesser extent, shear zones have been proposed as potential geothermal targets in ancient crystalline settings away from areas experiencing volcanism or rifting (Caspari et al., 2020). In detail, the potential of shear zones as deep geothermal prospects is significantly influenced by multiple processes that have adverse effects on the fluid flow properties of crystalline rocks. These processes include, for example, (i) the generation or clogging of pores due to mineral dissolution and precipitation, (ii) the formation of interparticle voids through material crushing and rotation, (iii) blockage of fluid pathways due to the migration of fine materials, and (iv) the compaction or rearrangement of fault gouge particles (Amitrano and Schmittbuhl, 2002; Johansen et al., 2008; Blöcher et al., 2016; Hofmann et al., 2016; Kluge et al., 2021). It's noteworthy that the brecciation and hydrothermal alteration processes responsible for shaping the described granitic reservoirs also play a significant role in the formation and location of mesothermal ore deposition (Sibson, 2004). In our specific case, the ages of shear zones that governed Au-mineralization in Northern Finland cluster around 1.8Ga (e.g. Molnár et al., 2018), suggesting a potential coeval formation with the observed secondary porosity.

On larger scales, spanning from tens of meters to kilometers, the architecture of brittle shear zones mirrors the response of rocks to tectonic stresses. This results in a diverse range of structural features and deformation patterns, often organized into characteristic arrays or networks. The terms 'single fault core' and 'multiple fault core' are employed to differentiate between the arrangements of faults and their associated damage zones. A 'single fault core' shear zone refers to a primary fault plane along which most displacement or sliding has occurred. In contrast, a 'multiple fault core' shear zone consists of several fault strands that interact with one another, forming a network of faults within a broader zone of deformation (e.g. Faulkner et al., 2008; Mitchell and Faulkner, 2009). Understanding the spatial and geometric distribution of these arrays is crucial for assessing the large-scale hydraulic properties of shear zones and their potential as geothermal reservoirs.

Multiple faults and rocks characteristic of fault core (breccias and cataclasites) intersect the Koillismaa drillhole, typically occurring as zones of up to 30m wide and often associated with mineral alteration of varying degrees (Fig. 1). These deformation/alteration zones account collectively for nearly 40 % of the total studied interval. Given the substantial number of faults distributed throughout the borehole, we have chosen to employ a 'multiple fault core' model to elucidate the location, interconnectivity, and geometric attributes of potential crystalline reservoirs within hydrothermally altered shear zones (Fig. 7). In this prospective model, the multiple shearing cores form anastomosing strands of fault rocks (e.g. Faulkner et al., 2008; Fossen et al., 2017), comprising permeable breccias, cataclasites, and fractured rocks (lithofacies 2b and 3; Fig. 7), as well as less permeable fault gouge and pseudotachylyte material. As the permeability of crystalline rocks typically increases due to brittle shearing (Kluge et al., 2021), it facilitates localized fluid percolation, leading to mineral alteration (lithofacies 2c and 4) and widespread secondary mineralization, which can impact any rocks within and adjacent to the shear zone. In addition to fault-related geothermal systems (Ledésert et al., 2009; Duwiquet et al., 2021), these processes and resulting pore-types are also documented in high-temperature geothermal systems associated with magmatic intrusions (Wyering et al., 2014; Stimac et al., 2019). Lenses of mechanically/chemically damaged (lithofacies 2abc and 4) and massive rocks (lithofacies 1) are found both within the shear zone and at its boundaries (Fig. 7). Overall, the porosity and deep permeability (at 50MPa for reference) increase from massive (lithofacies 1) to altered granites (lithofacies 4), whereas the bulk density, P-wave velocity, and thermal conductivity decrease (Fig. 7). This model only serves as a working hypothesis for assessing the potential of hydrothermally altered shear zones as deep geothermal reservoirs. The accuracy and applicability of the model (Fig. 7) may be subject to variations on a case-by-case basis.

6.3. Implication for geothermal exploration in crystalline settings

Our findings carry significant implications for upcoming geothermal exploration initiatives. Particularly noteworthy, our discovery that porosity may remain open for time spans over a billion years could mark a groundbreaking concept for the development of geothermal resources in ancient crystalline cratons. Presently, the prevailing geothermal exploration perception has been that fractures and pores of Precambrian shield rocks tend to be sealed through the precipitation of secondary minerals—an assumption that our dataset challenges. Further, our study emphasizes that, alongside fractures, the presence of interconnected moldic, sieve, and interparticle pores significantly enhances the quality of granitic reservoirs. The most promising reservoir properties were found in granites that underwent cataclasis and hydrothermal alteration, leading to a high porosity of nearly 20 % and a high permeability of $\sim 5 \times 10^{-14}$ m^2 (50mD), even when subjected to high confining pressures of 50MPa (~2km). Conversely, granites dominated by open regular fractures, while possessing extremely high permeability at shallow depths ($\sim 10^{-12}$ m^2 = 1 Darcy), cannot sustain substantial fluid flow as the confining pressure (i.e. depth) increases (Fig. 6f). The reduction in fracture transmissivity with depth is understood as a decrease in fracture aperture size, particularly when the lithostatic pressure surpasses 10–20MPa, corresponding to depths around 350–700m (Zangerl et al., 2008; Achtziger-Zupančič et al., 2017). We observe that this phenomenon is evident only on open regular fractures, whereas irregular fractures and altered/brecciated granites exhibit comparatively milder permeability reductions as confining pressure increases (Fig. 6f), emphasizing the significance of the pore-network morphology in the performance of deep geothermal reservoirs. This observation holds great importance for the advancement of EGS, which could prioritize the establishment of more intricate fracture networks through the implementation of thermal and chemical enhancement. In turn, chemical enhancement presents novel opportunities for co-producing critical metals like lithium and rubidium, for example, as well as high-density energy gases such as hydrogen and helium. These valuable elements are byproducts of the alteration processes of minerals such as biotite and plagioclase, and are commonly encountered in geothermal brines within crystalline rocks

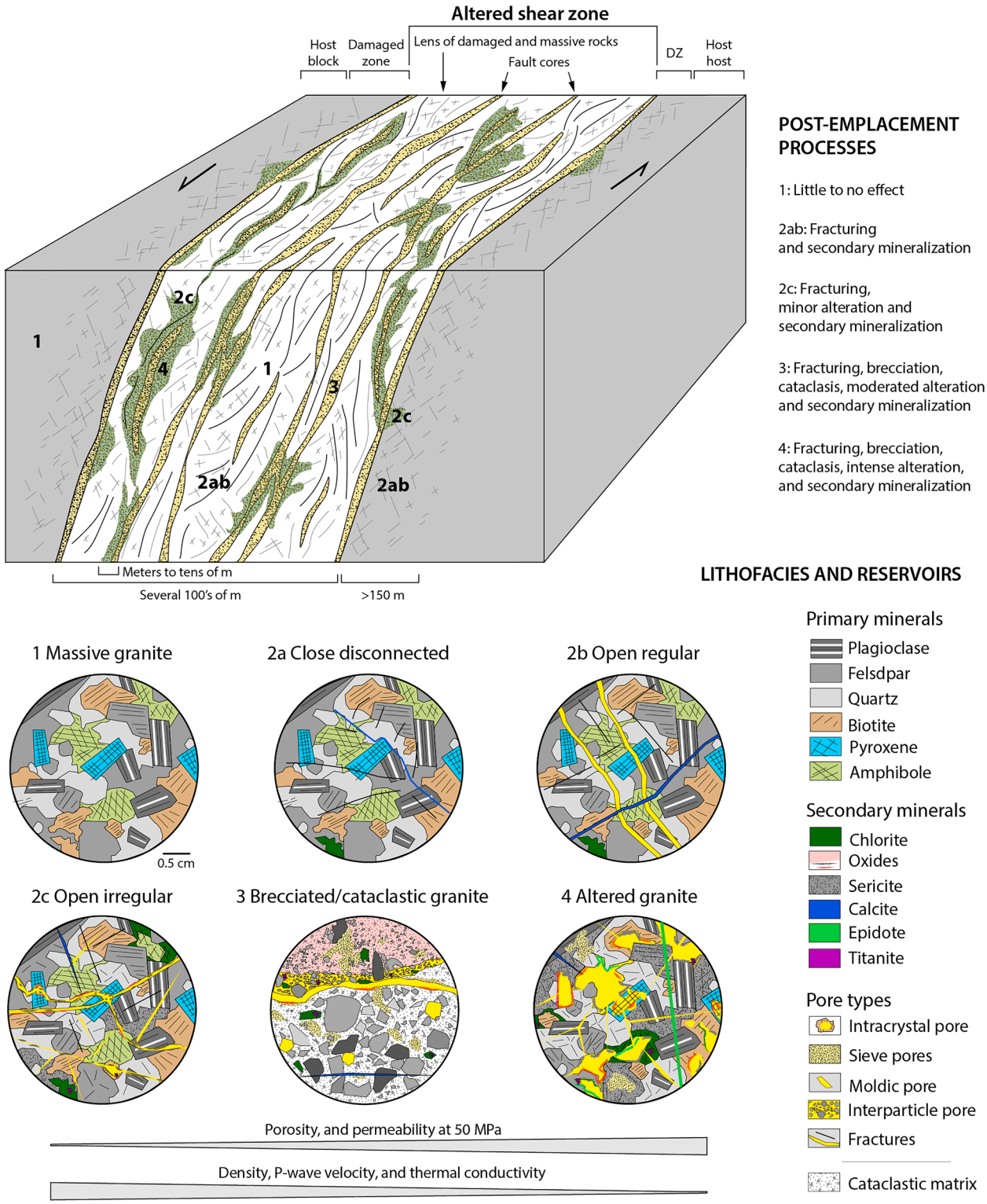

Fig. 7. Conceptual facies-structural model for the formation, distribution, sizes, and connectivity of granitic reservoirs within a shear zone that has undergone hydrothermal alteration. Shear zone architecture based on Faulkner et al. (2008) and Mitchell and Faulkner (2009). Reservoir quality increases as a result of the pore network morphology, which is in turn influenced by the original composition of the rock following magma crystallization and the extent of subsequent modification through various post-emplacement processes. The grey bars in the bottom part of the figure represent the trends for each thermal and petrophysical parameter analyzed.

(Murray et al., 2020; Sanjuan et al., 2022). Since these alteration types are observed in our dataset, it is possible that geothermal brines of hydrothermally altered shear zones may be enriched on these critical elements.

7. Conclusions

The potential of fault and shear zones as deep geothermal reservoirs remains largely untapped in crystalline settings. While fracture

permeability is recognized as a critical factor in creating prolific crystalline reservoirs within these zones, the effects of associated processes such as brecciation and mineral alteration have received limited attention. Our study revealed the presence of granitic reservoirs occurring at depths of nearly 2km within the Fennoscandian Shield. At a confining pressure of 50MPa (simulating their present depths), these granitic reservoirs exhibit a high porosity of nearly 20 % and a high permeability of $\sim 5 \times 10^{-14}$ m^2 (50mD). Brecciation, cataclasis, fracturing, and mineral dissolution collectively contribute to the creation of these exceptional reservoir properties, which have been widely overlooked in deep and ancient (over a billion years) crystalline settings. Our study demonstrates that brittle shearing and high-temperature (~200–300 °C) hydrothermal alteration are key factors in the formation of granitic reservoirs. These processes are typical of brittle shear zones, which have the potential to create extensive (>100m) interconnected crystalline reservoirs. Our findings unveil a new reservoir play for expanding geothermal energy production in crystalline terrains globally: brittle shear zones that have undergone propylitic alteration. Developing geothermal resources associated with these altered shear zones stands to make a substantial contribution to our ongoing shift towards cleaner and more reliable energy sources.

8. Methods

We use a multidisciplinary approach to investigate the formation of granitic reservoirs. The methods used in our work are separately described in further sections and include (i) drill core description, (ii) optical microscopy, (iii) hyperspectral imaging (HSI), (iv) computed tomography scanning (CT-scan), (v) micro X-ray fluorescence spectrometry (Micro-XRF), and (vi) petrophysical laboratory experiments (i.e. porosity, permeability, density, elastic wave velocity, and thermal conductivity). These complementary methods helped us to determine the main petrophysical and thermal trends of granitic rocks and assess their reservoir performance at progressive depths.

8.1. Drill core description and sample collection

We logged the deepest 472m (1250–1722m) section of the Koillismaa Deep Drillhole at a centimeter scale, collecting information about the texture, structure, composition, and mineral alteration aspects of key rock types. As core recovery was typically above 90 %, nearly continuous observation was possible. Thirty-two representative samples were collected from ultramafic and granitic lithologies as full core samples 50mm in diameter and lengths varying from 2 to 15cm. Further, petrographic, petrophysical, and mineral analytical characterization were carried out on selected samples, focusing on a subset of 25 granitic samples selected for detailed tests. From this granitic subset, 20 samples were selected for petrophysical tests, 10 for optical microscopy, 8 for Micro-XRF analysis, and 7 for CT-Scan imaging (Appendix 1).

8.2. Structural analysis

Regional lineament interpretation was performed using a highly accurate low-altitude airborne LiDAR-based topographical digital elevation model (DEM) collected by the National Land Survey of Finland. GTK processed this high-resolution LiDAR point cloud database into a DEM that represents the bare earth surface, meaning, it does not account for vegetation. The point density for the cloud data was set at 0.5 points per square meter, resulting in an elevation accuracy of 0.3m. The interpretation was done according to procedures defined in Nordbäck et al. (2023). The points were then triangulated to form a terrain surface mesh and subsequently interpolated with the natural neighbor algorithm into a 2m grid-size DEM raster. Lineament interpretation was performed at a single scale of observation with a representative fraction of 1:200.000. This interpretation was used to produce rose diagrams that represent the spatial orientation of regional structures near the drillhole site.

In addition to regional lineament interpretation, structural data were collected from the oriented core by (i) manual extraction using standard internal core angle measurements and (ii) the Reflex IQ logger device. The handheld Reflex IQ logger measures the orientation of the structures using a laser. Some sections of the core were intensely fractured and thus not possible to obtain a reliable orientation of the core, particularly in the ultramafic interval. Due to this limitation, at certain depths, our drill core observations can only provide an approximation of the main fault trends, which did not impact our first-order structural interpretation across the studied interval.

RQD (Rock Quality Designation) data was collected from the entire borehole length over 1m length intervals. RQD data measure a percentage of intact drill core sections 10cm or longer, thus, 100 % RQD indicates an intact drill core interval and the value provides a simple and efficient way to estimate the overall intactness of the rock, indicating the degree of joints, faults, and fractures within the drill core.

8.3. Optical microscopy

We performed detailed petrographic descriptions aiming to assess the main mineralogical, textural, and structural aspects of representative rock types. In addition, key petrographic features such as mineral shapes and intergrowth, secondary mineral replacement, and cataclastic grain-size reduction, helped us to identify critical syn- and post-emplacement processes, including the magmatic crystallization series, hydrothermal alteration processes, and brittle deformation courses. Seventeen thin sections were prepared at the University of Turku rock laboratory (10 from granites and 7 from ultramafic rocks). The rock samples were immersed in a solvent-free adhesive (Araldite) to avoid rock fragmentation and desegregation during cutting and thin-sectioning preparation. The Araldite adhesive was impregnated with yellow-fluorescent pigment to facilitate the identification and description of diverse pore types. Thin-section descriptions were performed using a Leitz Laborlux 11 POL microscope with 40 × maximum amplification coupled with a Euromex VC.3036 Ultra Color camera set to collect high-definition photographs of 3264 × 1836 megapixel size.

Optical microscopy also supported the pore morphology characterization of the igneous rocks and their formation processes. Our pore morphology classification was adapted and expanded from schemes proposed by Choquette and Pray (1970) and Sruoga and Rubinstein (2007) for sedimentary and volcanic rocks. It highlights nine fundamental pore types of granitic rocks including (i) moldic, (ii) sieve, (iii) interparticle, (iv) intracrystal, (v) vug, (vi) open regular fracture, (vii) open irregular fracture, (viii) closed disconnected fracture, and (ix) microfractures, the latest defined as fractures <0.5mm aperture. This petrographic dataset was then recorded and compared to complementary results from micro-XRF, hyperspectral analysis, and CT-scan imaging.

8.4. Hyperspectral analysis

Hyperspectral imaging is a non-invasive method that provides information about the mineralogical, mineral chemical composition, and structural aspects of rocks. This method records different wavelengths of the electromagnetic spectrum of the samples in tens to hundreds of bands. GTK acquired hyperspectral data from the Koillismaa Deep Drillhole in 2021–2022 using a SisuROCK drill core scanner with Specim RGB, FENIX, and OWL hyperspectral cameras. The data were acquired from air-dry samples at room temperature with a resolution of ~1.5mm pixel size in the visible (480–700nm), near-infrared (700–1300nm), short-wave infrared (1300–2500nm), and long-wave infrared (7500–12,000nm) wavelength regions. In addition, high-resolution (0.15mm) RGB (red, green, blue) data were acquired from the drill cores. Here, only RGB and FENIX data were used.

For the purposes of this work, the focus was placed on chlorite abundance using scalar D2250 (e.g. McLeod et al., 1987) extracted using

IntelliCore® software by Terracore, only evaluating the spectra of the granitic rocks. Scalars are extracted in IntelliCore® by applying a continuum removal to the spectral signatures (hull quotient from 1300nm to 2450nm) before defining the depth of the spectral minima (D). The defined window for searching D2250 minima in the spectra is from 2232nm to 2285nm. Numerical values for scalars are generated by taking a mean value across each 10cm interval of the image dataset. D2250 is developed also for biotite and epidote, although to a lesser degree than for chlorite (Laukamp et al., 2021). Since biotite is also absent from the best-developed reservoirs in our dataset, the absence of D2250 can be used as a proxy for exploring areas of potential porosity, as well as opened versus mineralized fractures, and rock structures such as brecciation (Fig. 1). As the hyperspectral images are collected from drill cores, the method cannot distinguish natural fractures from those originated by drilling. Thus, interpretation from hyperspectral imaging must be validated by complementary information from drill core description, petrography, and analytical techniques (e.g. Micro-XRF). Overall, granitic rocks displaying hot colors highlight the presence of secondary mineralization, closed fractures, and massive rocks, while cold colors show rock fragmentation, pores, and open fractures (Fig. 1).

8.5. Micro-XRF quantification

Micro-XRF analysis of seven samples was obtained at the GTK Research Laboratory in Espoo (Appendix 1). Micro-XRF is a non-destructive analytical technique used to determine the elemental composition of a sample at a microscopic scale. It is based on the principle of X-ray fluorescence, where a material is irradiated with X-rays. By measuring the energy and intensity of the emitted X-rays, the elements present in the sample can be detected and quantified. We primarily aimed to analyze the sample's mineral phases and alterations, textures, and compositions. Secondarily, we tested the performance of micro-XRF data coupled with AMICS quantification (Advanced Mineral Identification and Characterization System) to verify the pore space distribution of our samples. These data were compared with deterministic results from CT scans and petrophysical measurements including gas pycnometry and drill core water saturation tests, techniques that are described in detail in the further sections.

We use a Bruker Micro-XRF M4 Tornado plus with AMICS instrument equipped with a 30W rhodium (Rh) anode X-ray tube and two 30mm^2 silicon drift detectors (SDDs) with a resolution of <145eV (MnKα) at 275kcps (kilo counts per second). The Rh X-ray source was operated at maximum energy settings (50kV, 600 μA) and a polycapillary lens focused the beam to a fixed spot size of 20 μm under a 2mbar vacuum. Elemental mapping of the samples was performed using a step size of 20 μm and a pixel dwell time of 20ms. Qualitative elemental maps were generated for all samples using the Bruker M4 software equipped with the AMICS package. Bruker AMICS offers automated mineralogical analysis and image processing tools for quantitative mineral identification, grain boundary detection, particle size analysis, and mineral mapping. We utilize techniques such as image segmentation, pattern recognition, and statistical analysis to extract meaningful information from digital images of samples obtained through micro-XRF analysis. By using χ^2 fingerprinting for a best-match mineral classification, we compared our collected micro-XRF datasets with a reference list of known mineral spectra embedded into the AMICS software. This initial comparison guided our mineral recognition and classification, which was further refined using various clustering techniques and manual manipulation of XRF spectral attributes. The data was repeatedly reclassified to resolve X-ray points that were initially unclassified (i.e. determined as unknown elements), following methods presented in Bruker (2018).

Our final micro-XRF quantification product is a series of mineral and pore-class maps presenting a single class label or class mixtures per 20 μm pixel resolution, not exciting 2 % of unknown points. These maps allow us to quantify the relative mineral and pore distribution within our samples, which aided our rock classification using QAP (quartz vs. alkali feldspar vs. plagioclase) and feldspar types (albite vs. anorthite vs. orthoclase) diagrams (Appendix 1). This method was particularly important to determine the primary mineral composition of our rock samples and to assess the post-emplacement processes that have created pore-type variations within our rock dataset. Most granitoids were mineralogically classified as classic granites, although minor granodiorite and quartz-monzonite variations also occur (Fig. 2; Table 1). For this study, we refer to these granitoids simply as "granites".

8.6. CT scanning

CT scans provide information about the internal structure, composition, and density variations of rock samples. The technique uses X-rays to create detailed 3D reconstructions of the interior of the rocks. In our study, tomography analysis of the drill cores was used to characterize and quantify parameters such as pore morphology, distribution, and connectivity. In addition to the pore network data, the tomographic images helped us assess critical minerals and their altered variations. CT scans were collected at GTK's X-ray Computed Tomography Laboratory in Espoo using a GE Phoenix v|tome|x scanner. The samples were scanned using a helical trajectory in which the sample rises while it rotates. For the first set of lower-resolution scans, seven rock cylinders of various lengths by 50mm in diameter were scanned using an accelerating voltage of 150kV and a tube current of 225 μA, resulting in a total power of 33.75W. Copper and aluminum sections of 0.5mm were used as beam filters, and the obtained spatial resolution of the images was 30 μm. At each angle, the detector waited for a single exposure time and then took an average of 2–3 exposures. The single exposure time was set as 1 s, and there were 4647–7386 projections taken, resulting in a total scanning time of 310–388min per sample.

From these initial lower-resolution scans, zones of interest were selected for further assessment. After a preliminary analysis of the pore distribution and potential weak parts of the rocks that could be damaged during rock preparation, seven smaller rock cylinders measuring 40mm in length by 19.8mm in diameter were cut (Appendix 1). The CT scanning parameters were set as per the lower-resolution dataset, except that the tube current was changed to 75 μA, and the power to 11.25W, now using 0.1mm of copper as a beam filter. The spatial resolution was 11 μm, averaging 3 exposures each time, with a single exposure time of 0.5s, obtaining 4691–5695 projections for a total scan time of 156–190 min. From this higher-resolution dataset, the images were segmented using the Mask Segmentation and 2-Phase Watershed Segmentation recipes of ThermoFisher PerGeos 2020.2. Low-density regions corresponding to void volumes within the rock cylinders were colored to facilitate the visualization of the pores. Pore connectivity was then studied using the Labeling tool to assign a different label/value to each connected pore body, resulting in images where all pores of the same color are connected at a limit of 11 μm in diverse zones of the rock sample.

8.7. Petrophysical measurements

Density, connected porosity, P-wave velocity, and thermal conductivity were conducted at the University of Strasbourg and GTK laboratories, while measurements of sample porosity and permeability as a function of confining pressure were performed at the University of Strasbourg. Appendix 1 presents a detailed compilation of the methods and tests applied for each sample and their respective results.

8.7.1. Experiments performed at the Strasbourg Institute of Earth & Environment (University of Strasbourg, France)

All of the samples measured in Strasbourg were 19.8mm-diameter cylinders with a nominal length of 40mm. Samples containing large fractures were wrapped in adhesive tape for the measurements of P-wave velocity, thermal conductivity, and permeability.

The samples were first vacuum-dried in a vacuum oven at 40 °C for at least 48h. The bulk density of the samples measured in Strasbourg was determined using the dry mass, measured using a digital balance (accuracy of 0.001g), and the sample dimensions, measured using digital calipers (accuracy of 0.01mm). The effective porosity (sometimes called connected or open porosity) was measured using the bulk sample volume (calculated using the sample dimensions) and the skeletal volume was measured using a helium pycnometer (Micromeritics AccuPyc II; accuracy of 0.0001cm^3). P-wave velocity was measured on dry samples using two piezoelectric sensors, a function generator (Agilent Technologies 33210A, 10 MHz function/waveform generator), a signal amplifier, and an oscilloscope (Agilent Technologies DSO5012A digital storage oscilloscope). A schematic diagram of the device can be found in Heap et al. (2014). P-wave velocity was measured along the axis of each of the samples (using a frequency of 700kHz) under ambient laboratory pressure and temperature. To ensure a good connection between the sample and the endcaps, we applied an axial force of 300N. Thermal conductivity was measured using a Hot Disk® 500 Thermal Constants Analyzer using the transient plane source method (Gustafsson, 1991; Heap et al., 2020). The TPS method uses a resistive sensor (the transient plane source) sandwiched between two samples to measure the increase in resistance as it heats the samples using an electrical current pulse. In our setup, the resistive sensor consists of two 10 μm-thick nickel foil spirals (radius of 3.189mm) that are encased and insulated by 30 μm-thick Kapton. Measurements were made by sandwiching the sensor between the cylindrical sample to be measured and a piece of high-porosity foam with a very low thermal conductivity. A good contact between the sensor and the surface of the sample was ensured by tightening a screw positioned at the top of the sample jig. The standard error for the thermal conductivity measured using our Hot Disk® TPS 500 Thermal Constants Analyzer, assessed by measuring the same sandstone sample 100 times, was found to be 0.007W m^{-1} K^{-1} (Heap et al., 2023).

Permeability measurements were performed at the ITES Rock Physics laboratory on five samples that were submitted to increasing confining pressure from 1 to 50MPa. Confining pressures are commonly used to simulate the conditions deep within the Earth's crust. Here, confining pressure was applied to simulate the permeability of the rocks at increasing depths from 0 to ~2km, considering a constant crustal density of 2.6kg/cm^3, typical of crystalline terrains. Gas (argon) permeability measurements were performed in a high-pressure vessel (50MPa) at room temperature on cores 40mm long and 19.8mm in diameter. Samples were vacuum-dried at 40 °C for 12h, and then jacketed in a Viton sleeve and placed inside the pressure vessel. The confining pressure was then increased to 1MPa and left for 24h at this pressure to allow for microstructural equilibration. Argon permeability was measured using either the steady-state method or the pulse-decay method depending on the permeability of the sample. For the steady-state method (high permeability of $>10^{-16}$ m^2), a constant pressure gradient was imposed across the sample and the outlet flow rate was measured using a flowmeter. Permeability was then derived from a modified Darcy's law designed to estimate the flow rate of compressible fluids (Scheidegger, 1974). For the pulse-decay method (used for the lower permeability samples; $<10^{-16}$ m^2), the decay of the initial pressure gradient was monitored after the closure of the upstream pore fluid inlet, the downstream pressure being in all cases the atmospheric pressure. A local application of Darcy's law to the interface between the upstream gas reservoir and the sample thus leads to the permeability of the sample (Brace et al., 1968). When Darcy's law was no longer valid, a correction was introduced to the measured values because either inertial effects appear at high flow rates (Forchheimer correction) or gas slippage appears along the pore walls at low permeability (Klinkenberg correction). The process was repeated for each confining pressure level by respecting the 12h equilibration period, resulting in a total experiment time of ~240h per sample. We highlight that our permeability measurements were performed on 19.8mm-diameter cores and so our values of permeability are representative of the matrix. Permeability on the rock-mass scale would be higher than the values quoted herein, due to the presence of permeability-enhancing meso- and macroscale fractures.

The porosity of the 19.8mm-diameter core of the altered granite (Koi-01b) was measured as a function of confining pressure in a hydrostatic pressure vessel (a type of experiment often referred to as a "hydrostat"). This sample was first vacuum-saturated with deionized water, inserted into a Viton sleeve, and placed inside the pressure vessel. The confining and pore fluid pressure was then increased to 2 and 1MPa, respectively, using servo-controlled pumps, and the sample was left overnight to ensure microstructural equilibration. The following morning, the confining and pore fluid pressure was slowly increased to 12 and 10MPa, respectively, and the sample was again left to equilibrate. The volume of deionized water in the sample was monitored during the experiment using an encoder incorporated into the servo-controlled pore fluid pressure pump. Once the volume of water within the sample was constant for a protracted duration, the sample was considered to have fully equilibrated to the starting effective pressure of 2MPa (we assume here a simple effective pressure law in which the effective pressure is equal to the confining pressure minus the pore fluid pressure). The confining pressure was then increased at a constant rate of ~10MPa/h to a maximum of 50MPa. During pressurization, the change in the volume of water within the sample, converted to a porosity change using the sample dimensions, was monitored and recorded. This experiment therefore provides the porosity reduction as a function of effective confining pressure.

8.7.2. *Experiments performed at the GTK laboratory (Finland)*

At the GTK laboratory, 14 polished discs of 7 × 50mm and 2 cylindrical samples of 30 × 50mm were prepared for density, connected porosity, P-wave velocity, and thermal conductivity measurements. Initially, the samples were washed and oven-dried for 72h at a temperature of 40 °C. Due to the fragility of fractured and altered samples, they were wrapped in adhesive tape before the measurements of P-wave velocity and thermal conductivity.

The bulk density of the samples was determined using the Archimedean principle by measuring the mass of the samples in the air and water. These measurements were conducted at a temperature of approximately 20 °C using a precision scale with an accuracy of 0.01g. The connected porosity of the samples was also determined using the Archimedean principle, using the "triple-weight" water-saturation method. To do so, the samples were first immersed in water for 72h and their wet mass was measured in air and suspended underwater using a precision scale with an accuracy of 0.01g. The samples were then dried for 48h at a temperature of 105 °C and their dry mass was measured using the same precision scale. The connected porosities of the samples were then calculated using Archimedes' principle. P-wave velocity was measured under wet conditions using a device developed by GTK. This device operates by measuring the propagation time of a high-frequency (1MHz) acoustic pulse across the samples. The pulse generator emits an acoustic pulse that traverses the sample, and the travel time is precisely measured with a pulse counter. The accuracy of the method is approximately 10m/s, ensuring reliable results. Finally, the samples were soaked in water for a duration of 14 days, and thermal conductivity tests were conducted under wet conditions using the divided bar method (Beck, 1988). In this method, the sample is positioned at the center of a vertical column consisting of alternating quartz and copper discs. Initially, the top and bottom of the column were maintained at constant temperatures, and subsequently, a differential temperature of 10 °C was applied. This temperature difference generates a heat flux through both the column and the sample. Temperature variations are recorded from the quartz and copper materials and the sample itself. The thermal conductivity of the samples is then calculated using Fourier's law. The samples were then air-dried at room temperature for approximately 90 days and their thermal conductivity was determined under dry conditions using the same method.

Minimal variations in the data measured in the two institutions (in France and Finland) were observed among samples belonging to the same lithofacies group (Appendix 1). Therefore, we conclude that the application of different methods at the two institutions did not significantly impact our first-order petrophysical and thermal interpretation of crystalline reservoirs.

Funding sources

A. Bischoff was funded by the research project "Deep-HEAT-Flows: Discovering deep geothermal resources in low-enthalpy crystalline settings", granted by the Research Council of Finland (#354356). A. Bischoff was also supported by GTK internal grants Koillismaa Deep Hole and Geoenergy Innovation. M.J. Heap was funded by the Interdisciplinary Thematic Institute GeoT, part of the ITI 2021-2028 program of the University of Strasbourg, CNRS and Inserm, supported by IdEx Unistra (ANR-10-IDEX-0002) and SFRI-STRAT'US project (ANR ANR-20-SFRI-001) under the framework of the French Investments for the Future Program. M.J. Heap was also supported by the Institut Universitaire de France (IUF) and by the ANR project GERESFAULT (ANR-19-CE05-0043). X-ray tomography (Jukka Kuva) and μXRF (Ester M. Jolis) were funded by the Academy of Finland through the RAMI infrastructure project (#293109 and #337560).

CRediT authorship contribution statement

Alan Bischoff: Conceptualization, Data curation, Formal analysis, Funding acquisition, Investigation, Methodology, Project administration, Resources, Supervision, Validation, Visualization, Writing – original draft, Writing – review & editing. **Michael J. Heap:** Conceptualization, Data curation, Formal analysis, Investigation, Resources, Supervision, Writing – original draft, Writing – review & editing. **Perttu Mikkola:** Conceptualization, Data curation, Formal analysis, Investigation, Resources, Supervision, Writing – original draft, Writing – review & editing. **Jukka Kuva:** Data curation, Formal analysis, Investigation, Methodology, Validation, Writing – original draft, Writing – review & editing. **Thierry Reuschlé:** Data curation, Formal analysis, Investigation, Methodology, Validation, Writing – original draft, Writing – review & editing. **Ester M. Jolis:** Data curation, Formal analysis, Investigation, Methodology, Validation, Writing – original draft, Writing – review & editing. **Jon Engström:** Data curation, Formal analysis, Visualization, Writing – original draft, Writing – review & editing. **Heini Reijonen:** Data curation, Formal analysis, Methodology, Validation, Writing – original draft, Writing – review & editing. **Tuomas Leskelä:** Data curation, Formal analysis, Validation.

Declaration of competing interest

The authors declare that they have no known competing financial interests or personal relationships that could have appeared to influence the work reported in this paper.

Acknowledgments

We thank Satu Vuoriainen (GTK) and Toni Luoto (GTK) for their diligent work with our challenging fractured and altered samples, and Arto Peltola (University of Turku) for providing us with outstanding quality thin sections that significantly enriched our research. We also appreciate the contributions of Nikolas Ovaskainen (GTK) for his expertise in lineament mapping, GTK's geophysical team for their provision of petrophysical data, and Samuli Haavikko, Pertti Telkkälä and Jarmo Rauhala for RQD logging dataset. Dr. Phil Harris (Terracore) is thanked for providing valuable discussions regarding hyperspectral data interpretations, and Teppo Arola for the geothermal insights into low-enthalpy crystalline settings. We greatly appreciate the thorough review provided by two anonymous reviewers. All authors acknowledge the invaluable funding support that has made our scientific research possible.

Supplementary materials

Supplementary material associated with this article can be found, in the online version, at doi:10.1016/j.geothermics.2023.102895.

References

Achtziger-Zupančič, P., Loew, S., Mariéthoz, G., 2017. A new global database to improve predictions of permeability distribution in crystalline rocks at site scale. J. Geophys. Res. Solid Earth 122, 3513–3539. https://doi.org/10.1012/2017JB014106.

Amitrano, D., Schmittbuhl, J., 2002. Fracture roughness and gouge distribution of a granite shear band. J. Geophys. Res. Solid Earth 107 (B12). https://doi.org/10.1029/2002JB001761. ESE 19-1–ESE 19-16.

Anttilainen, T. (2023). Koillismaan syväreiän happamien kivilajien iänmääritys sekä geokemiallinen ja petrografinen luokittelu. University of Turku, M.Sc. thesis, 69 p. In Finnish with English abstract. https://urn.fi/URN:NBN:fi-fe2023032032543.

Atkinson, BK., 1984. Subcritical crack growth in geological materials. J. Geophys. Res. Sol. Earth 89, 4077–4114. https://doi.org/10.1029/JB089iB06p04077.

Beck, AE., Hanel, R., Rybach, L., Stegena, L., 1988. Methods for determining thermal conductivity and thermal diffusivity. Handbook of Terrestrial Heat Flow Density Determination. Kluwer, Dordrecht, pp. 87–124.

Bischoff, A., Fensom, J., Tang, H., Rosetti, M., Nicol, A., 2021. Processes Controlling Volcanic and Epiclastic Reservoir Formation in a Buried Polygenetic Stratocone. The Geological Society Special Publications SP520. https://doi.org/10.1144/SP520-2021-137.

Blöcher, G., Reinsch, T., Henninges, J., Milsch, H., Regenspurg, S., Kummerow, J., Francke, H., Kranz, S., Saadat, A., Zimmermann, G., Huenges, E., 2016. Hydraulic history and current state of the deep geothermal reservoir Groß Schnebeck. Geothermics 63, 27–43. https://doi.org/10.1016/j.geothermics.2015.07.008.

Bossennec, C., Géraud, Y., Böcker, J., et al., 2021. Evolution of diagenetic conditions and burial history in Buntsandstein Gp. fractured sandstones (Upper Rhine Graben) from *in-situ* δ18O of quartz and 40Ar/39Ar geochronology of K-feldspar overgrowths. Int. J. Earth Sci. (Geol. Rundsch) 110, 2779–2802. https://doi.org/10.1007/s00531-021-02080-2.

Brace, W., Walsh, J.B., Frangos, W.T., 1968. Permeability of granite under high pressure. J. Geophys. Res. 73, 2225–2236. https://doi.org/10.1029/JB073i006p02225.

Breede, K., Dzebisashvili, K., Liu, X., et al., 2013. A systematic review of enhanced (or engineered) geothermal systems: past, present and future. Geotherm. Energy 1, 4. https://doi.org/10.1186/2195-9706-1-4.

Brogi, A., Lazzarotto, A., Liotta, D., Ranalli, G., 2003. Extensional shear zones as imaged by reflection seismic lines: the Larderello geothermal field (central Italy). Tectonophysics 363, 1–2. https://doi.org/10.1016/S0040-1951(02)00668-6. VolumeIssues.

Brown, D., DuTeaux, R., Kruger, P., et al., 1999. Fluid circulation and heat extraction from engineered geothermal reservoirs. Geothermics 28, 553–572. https://doi.org/10.1016/S0375-6505(99)00028-0.

Bruker (2018), Mineral composition analysis using the M4 TornadoAmics. Lab report XRF 469 (Micro-XRF-application-note-XRF-469-mineral-composition-analysis-using-M4-TORNADO-AMICS-EN-BRUKER.pdf).

Cartwright-Taylor, A., Main, I.G., Butler, I.B., Fusseis, F., Flynn, M., King, A., 2020. Catastrophic failure: how and when? Insights from 4-D *in situ* X-ray microtomography. J. Geophys. Res. Sol. Earth 125, e2020JB019642. https://doi.org/10.1029/2020JB019642.

Caspari, E., Greenwood, A., Baron, L., Egli, D., Toschini, E., Hu, K., Holliger, K., 2020. Characteristics of a fracture network surrounding a hydrothermally altered shear zone from geophysical borehole logs. Solid Earth 11, 829–854. https://doi.org/10.5194/se-11-829-2020.

Clauser, C., Huenges, E., 1995. Ahrens T.J. Thermal conductivity of rocks and minerals. Rock Physics & Phase Relations: A Handbook of Physical Constants. American Geophysical Union. AGU Reference Shelf, pp. 105–126. https://doi.org/10.1029/RF003p0105. ISBN:9780875908533, ISBN:9781118668108.

Choquette, PW., Pray, L., 1970. Geologic nomenclature and classification of porosity in sedimentary carbonates. Am. Assoc. Pet. Geol. Bull. 54, 207–250.

Faulds, J., Hinz, N., Coolbaugh, M., Cashman, P., Kratt, C., Dering, G., Edwards, J., Mayhew, B., McLachlan, H., 2011. Assessment of favorable structural settings of geothermal systems in the Great Basin, Western USA. Trans. Geotherm. Resour. Council 35, 777–783.

Faulkner, DR., Mitchell, TM., Rutter, EH., Cembrano, J., 2008. On the Structure and Mechanical Properties of Large Strike-Slip Faults. In: On the Structure and Mechanical Properties of Large Strike-Slip Faults, 299. Geological Society, pp. 139–150. https://doi.org/10.1144/SP299.9. London, Special Publications.

Frey, M., Bär, K., Stober, I., et al., 2022. Assessment of deep geothermal research and development in the Upper Rhine Graben. Geotherm. Energy 10, 18. https://doi.org/10.1186/s40517-022-00226-2.

Fossen, H., Cavalcante, GCG., 2017. Shear zones – A review. Earth-Sci. Rev. 171 https://doi.org/10.1016/j.earscirev.2017.05.002. Volume.

Genter, A., Evans, K., Cuenot, N., Fritsch, D., Sanjuan, B., 2010. Contribution of the exploration of deep crystalline fractured reservoir of Soultz to the knowledge of Enhanced Geothermal Systems (EGS). Comptes Rendus Geosci. https://doi.org/10.1016/j.crte.2010.01.006.

Green, PF., Japsen, P., Bonow, LM., et al., 2022. The post-Caledonian thermo-tectonic evolution of Fennoscandia. Gondwana Res. 107, 201–234. https://doi.org/10.1016/j.gr.2022.03.007. VolumePages.
Gustafsson, S.E., 1991. Transient plane source techniques for thermal conductivity and thermal diffusivity measurements of solid materials. Rev. Sci. Instrum. 62 (3), 797–804. https://doi.org/10.1063/1.1142087.
Duwiquet, H., Guillou-Frottier, L., Arbaret, L., et al., 2021. Crustal Fault Zones (CFZ) as geothermal power systems: a preliminary 3D THM model constrained by a multidisciplinary approach. Geofluids. https://doi.org/10.1155/2021/8855632.
Griffiths, L., Heap, MJ., Baud, P., Schmittbuhl, J., 2017. Quantification of microcrack characteristics and implications for stiffness and strength of granite. Int. J. Rock Mech. Min. Sci. 100, 138–150. https://doi.org/10.1016/j.ijrmms.2017.10.013.
Gudmundsson, A., Berg, SS., Lyslo, KB., Skurtveit, E., 2001. Fracture networks and fluid transport in active fault zones. J. Struct. Geol. 23 (2–3), 343–353. https://doi.org/10.1016/S0191-8141(00)00100-0. VolumeIssuesPages.
Hampl, FJ., Schiperski, F., Byrne, JM., et al., 2022. The role of iron-bearing minerals for the deep weathering of a hydrothermally altered plutonic rock in semi-arid climate (Chilean Coastal Cordillera). Chem. Geol. 604 https://doi.org/10.1016/j.chemgeo.2022.120922. Volume.
Heap, M.J., Lavallée, Y., Petrakova, L., Baud, P., Reuschlé, T., Varley, N.R., Dingwell, D. B., 2014. Microstructural controls on the physical and mechanical properties of edifice-forming andesites at Volcán de Colima, Mexico. J. Geophys. Res. Solid Earth 119 (4), 2925–2963. https://doi.org/10.1002/2013JB010521.
Heap, MJ., Kennedy, BM., 2016. Exploring the scale-dependent permeability of fractured andesite. Earth Planet. Sci. Lett. 447, 139–150. https://doi.org/10.1016/j.epsl.2016.05.004.
Heap, M.J., Kushnir, ARL., Vasseur, J., Wadsworth, JB., Harlé, P., Baud, P., Kennedy, BM., Troll, VR., Deegan, F.M., 2020. The thermal properties of porous andesite. J. Volcanol. Geotherm. Res. 398 https://doi.org/10.1016/j.jvolgeores.2020.106901. Volume.
Heap, M.J., Wadsworth, F.B., Jessop, D.E., 2023. The thermal conductivity of unlithified granular volcanic materials: the influence of hydrothermal alteration and degree of water saturation. J. Volcanol. Geotherm. Res. 435, 107775 https://doi.org/10.1016/j.jvolgeores.2023.107775.
Hofmann, H., Blöcher, G., Milsch, H., Babadagli, T., Zimmermann, G., 2016. Transmissivity of aligned and displaced tensile fractures in granitic rocks during cyclic loading. Int. J. Rock Mech. Min. Sci. 87, 69–84. https://doi.org/10.1016/j.ijrmms.2016.05.011.
Hölttä, P., Heilimo, E., Nironen, M., 2017. Bedrock of Finland at The scale 1: 1 000 000 – Major Stratigraphic Units, Metamorphism and Tectonic Evolution. Geological Survey of Finland, pp. 77–128. Special Paper 60.
Hölttä, P., Mänttäri, I., Huhma, H., Kurhila, M., Ruotoistenmäki, T., Kontinen, A., 2021. Growth of the Archean sialic crust as revealed by zircon in the TTGs in eastern Finland. Bull. Geol. Soc. Finland 93, 77–104. https://doi.org/10.17741/bgsf/93.2.001.
Huigen, Y., Andriessen, P., 2004. Thermal effects of Caledonian foreland basin formation, based on fission track analyses applied on basement rocks in central Sweden. Phys. Chem. Earth 10, 29. https://doi.org/10.1016/j.pce.2004.03.006. Parts A/B/CVolumeIssue.
Laajoki, K., 2005. Karelian Supracrustal Rocks. Developments in Precambrian Geology, 14. Elsevier. https://doi.org/10.1016/S0166-2635(05)80008-8. Volume.
Johansen, T.E.S., Fossen, H., Wibberley, C.A.J., Kurz, W., Imber, J., Holdsworth, R.E., Collettini, C., 2008. Internal geometry of fault damage zones in interbedded siliciclastic sediments. The Internal Structure of Fault Zones: Implications for Mechanical and Fluid-Flow Properties, 299. Geological Society, Special Publications, London, pp. 35–56. https://doi.org/10.1144/SP299.3.
Jolie, E., Scott, S., Faulds, J., et al., 2021. Geological controls on geothermal resources for power generation. Nat. Rev. Earth Environ. 2, 324–339. https://doi.org/10.1038/s43017-021-00154-y.
Inskip, N.F., Harpers, N., Shail, R., et al., 2023. Reservoir properties of fault-related hydrothermally altered granites in Cornwall: implications for geothermal energy prospectivity. ESS Open Archive. https://doi.org/10.22541/essoar.170110671.11387934/v1.
Kärenlampi, K., Kontinen, A., Huhma, H., Hanski, E., 2019. Geology, geochronology and geochemistry of the 2.05 Ga gneissic A1-type granites and related intermediate rocks in central Finland: implication for the tectonic evolution of the Karelia craton margin. Bull. Geol. Soc. Finland 91, 35–73. https://doi.org/10.17741/bgsf/91.1.002.
Kluge, C., Blöcher, G., Barnhoorn, A., et al., 2021. Permeability evolution during shear zone initiation in low-porosity rocks. Rock Mech. Rock Eng. 54, 5221–5244. https://doi.org/10.1007/s00603-020-02356-0.
Kontinen, A., Paavola, J., Lukkarinen, H., 1992. K–Ar ages of hornblende and biotite from Late Archaean rocks of eastern Finland — interpretation and discussion of tectonic implications. Geol. Surv. Finland Bull. 365, 31.
Kontinen, A., Huhma, H., Lahaye, Y., O'Brien, H., Hölttä, P., 2013. Current Research: GTK Mineral Potential Workshop. Geological Survey of Finland. Report of Investigation, pp. 70–74. Kuopio198.
Kohonen, J., Rämö, OT., 2005. Sedimentary rocks, diabases, and late cratonic evolution. Precambrian Geology of Finland. Elsevier Scientific Publ. Co., pp. 563–604. https://doi.org/10.1016/S0166-2635(05)80014-3
Kraal, K.O., Ayling, B.F., Blake, K., et al., 2021. Linkages between hydrothermal alteration, natural fractures, and permeability: integration of borehole data for reservoir characterization at the Fallon FORGE EGS site, Nevada, USA. Geothermics 89. https://doi.org/10.1016/j.geothermics.2020.101946. Volume.
Kukkonen, I., Heikkinen, P., Malin, P., et al., 2023. Hydraulic conductivity of the crystalline crust: Insights from hydraulic stimulation and induced seismicity of an enhanced geothermal system pilot reservoir at 6 km depth, Espoo, southern Finland. Geothermics 112. https://doi.org/10.1016/j.geothermics.2023.102743. Volume.
Kushnir, A.R.L., Heap, M.J., Baud, P., et al., 2018. Characterizing the physical properties of rocks from the Paleozoic to Permo-Triassic transition in the Upper Rhine Graben. Geotherm. Energy 6, 16. https://doi.org/10.1186/s40517-018-0103-6.
Ledésert, B., Hebert, R., Genter, A., Bartier, D., Clauer, N., Grall, C., 2009. Fractures, hydrothermal alterations and permeability in the Soultz enhanced geothermal system. Comptes Rendus Geosci. 342 (7-8) https://doi.org/10.1016/j.crte.2009.09.011. VolumeIssues.
Laukamp, C., Rodger, A., LeGras, M., Lampinen, H., Lau, I.C., Pejcic, B., Stromberg, J., Francis, N., Ramanaidou, E., 2021. Mineral physicochemistry underlying feature-based extraction of mineral abundance and composition from shortwave, mid and thermal infrared reflectance spectra. Minerals 11, 347. https://doi.org/10.3390/min11040347, 2021.
Lauri, L.S., Mikkola, P., Karinen, T., 2012. Early Paleoproterozoic felsic and mafic magmatism in the Karelian province of the Fennoscandian shield. Lithos 151, 74–82. https://doi.org/10.1016/j.lithos.2012.01.013.
Lauri, L.S., Rämö, O.T., Huhma, H., Mänttäri, I., Räsänen, J., 2006. Petrogenesis of silicic magmatism related to the 2. 44 Ga rifting of Archean crust in Koillismaa, eastern Finland. Lithos 86, 137–166. https://doi.org/10.1016/j.lithos.2005.03.016.
McBeck, J.A., Zhu, W., Renard, F., 2021. The competition between fracture nucleation, propagation, and coalescence in dry and water-saturated crystalline rock. Solid Earth 12, 375–387. https://doi.org/10.5194/se-12-375-2021.
McLeod, R.L., Gabell, A.R., Green, A.A., Gardavsky, V., 1987. Chlorite infrared spectral data as proximity indicators of volcanogenic massive sulphide mineralisation. In: The Australasian Institute of Mining and Metallurgy, Pacific Rim Congress, Melbourne, Proceedings, 87, pp. 321–324 v.p.
Meredith, P.G., Main, I.G., Clint, O.C., Li, L., 2012. On the threshold of flow in a tight natural rock. Geophys. Res. Lett. 39 (4) https://doi.org/10.1029/2011GL050649.
Mitchell, T.M., Faulkner, D.R., 2009. The nature and origin of off-fault damage surrounding strike-slip fault zones with a wide range of displacements: a field study from the Atacama fault system, Northern Chile. J. Struct. Geol. 31, 802–816. https://doi.org/10.1016/j.jsg.2009.05.002.
Molnár, F., Middleton, A., Stein, H., O'Brien, H., Lahaye, Y., Huhma, H., Pakkanen, L., Johanson, B., 2018. Repeated syn- and post-orogenic gold mineralization events between 1.92 and 1.76 Ga along the Kiistala shear zone in the Central Lapland Greenstone Belt, northern Finland. Ore Geol. Rev. 936–956. https://doi.org/10.1016/j.oregeorev.2018.08.015.
Mørk, M.B.E., Moen, K., 2007. Compaction microstructures in quartz grains and quartz cement in deeply buried reservoir sandstones using combined petrography and EBSD analysis. J. Struct. Geol. 29 (11) https://doi.org/10.1016/j.jsg.2007.08.004. VolumeIssue.
Murray, J., Clément, A., Fritz, B., Schmittbuhl, J., Bordmann, V., Fleury, J.M., 2020. Abiotic hydrogen generation from biotite-rich granite: A case study of the Soultz-sous-Forêts geothermal site, France. Appl.Geochem. 119 https://doi.org/10.1016/j.apgeochem.2020.104631.
Nasseri, M.H.B., Schubnel, A., Young, R.P., 2007. Coupled evolutions of fracture toughness and elastic wave velocities at high crack density in thermally treated Westerly granite. Int. J. Rock Mech. Min. Sci. 44 (4), 601–616. https://doi.org/10.1016/j.ijrmms.2006.09.008.
Nironen, M., Nironen, M., 2017. Bedrock of Finland at the Scale 1: 1 000 000 – Major Stratigraphic Units, Metamorphism and Tectonic Evolution. Geological Survey of Finland, pp. 41–75. Special Paper 60.
Nishimoto, S., Yoshida, H., 2010. Hydrothermal alteration of deep fractured granite: Effects of dissolution and precipitation. Lithos 115 (1-4). https://doi.org/10.1016/j.lithos.2009.11.015. VolumeIssues.
Nordbäck, N., Ovaskainen, N., Markovaara-Koivisto, M., Skyttä, P., Ojala, A., Engström, J., Nixon, C., 2023. Multiscale mapping and scaling analysis of the censored brittle structural framework within the crystalline bedrock of southern Finland. Bull. Geol. Soc. Finland 95 (1), 5–32. https://doi.org/10.17741/bgsf/95.1.001.
Pajunen, M., Poutiainen, M., 1999. Palaeoproterozoic prograde metasomatic-metamorphic overprint zones in Archaean tonalitic gneisses, eastern Finland. Bull. Geol. Soc. Finland 71, 73–132. https://doi.org/10.17741/bgsf/71.1.005.
Piipponen, K., Martinkauppi, A., Korhonen, K., Vallin, S., Arola, T., Bischoff, A., Leppäharju, N., 2022. The deeper the better? A thermogeological analysis of medium-deep borehole heat exchangers in low-enthalpy crystalline rocks. Geotherm Energy 10, 12. https://doi.org/10.1186/s40517-022-00221-7.
Editor(s) Rämö, O.T., Haapala, I., Lehtinen, M., Nurmi, P.A., Rämö, O.T., 2005. Chapter 12: Rapakivi granites. Developments in Precambrian Geology. Elsevier. https://doi.org/10.1016/S0166-2635(05)80013-1. Volume 14.
Rizzo, R.E., Healy, D., Heap, M.J., Farrell, N.J., 2018. Detecting the onset of strain localization using two-dimensional wavelet analysis on sandstone deformed at different effective pressures. J. Geophys. Res. Solid Earth 123 (12), 10–460. https://doi.org/10.1029/2018JB015898.
Samuelsson, J., Middleton, M.F., 1998. The Caledonian foreland basin in Scandinavia: constrained by the thermal maturation of the Alum Shale. GFF 120 (3), 307–314. https://doi.org/10.1080/11035899809453224.
Sanchez-Alfaro, P., Reich, M., Arancibia, G., et al., 2016. Physical, chemical and mineralogical evolution of the Tolhuaca geothermal system, southern Andes, Chile: Insights into the interplay between hydrothermal alteration and brittle deformation. J. Volcanol. Geotherm. Res. 324 https://doi.org/10.1016/j.jvolgeores.2016.05.009. Volume.
Sanjuan, B., Gourcerol, B., Millot, R., Rettenmaier, D., Jeandel, E., Rombaut, A., 2022. Lithium-rich geothermal brines in Europe: an up-date about geochemical

characteristics and implications for potential Li resources. Geothermics 101. https://doi.org/10.1016/j.geothermics.2022.102385. Volume.
Sausse, J., Genter, A., 2005. Types of Fracture Permeability in Granite. Geological Society London Special Publications, pp. 1–14. https://doi.org/10.1144/GSL.SP.2005.240.01.01.
Scheidegger, A., 1974. The Physics of Flow through Porous Media, 3rd Edition. University of Toronto Press. Toronto, Canada.
Schmid, S.M., Handy, M.R., 1991. Towards a genetic classification of fault rocks: geological usage and tectonophysical implications. Controversies in Modern. Academic Press, pp. 339–361. London.
Sibson, R.H., 2004. Controls on maximum fluid overpressure defining conditions for mesozonal mineralisation. J. Struct. Geol. 26 (6–7), 1127–1136. https://doi.org/10.1016/j.jsg.2003.11.003. VolumeIssuesPages.
Snowdon, A.P., Normani, S.D., Sykes, J.F., 2021. Analysis of crystalline rock permeability versus depth in a Canadian Precambrian rock setting. J. Geophys. Res. Solid Earth 126. https://doi.org/10.1029/2020JB020998.
Stanëk, M., Géraud, Y., 2019. Granite microporosity changes due to fracturing and alteration: secondary mineral phases as proxies for porosity and permeability estimation. Solid Earth 10, 251–274. https://doi.org/10.5194/se-10-251-2019.
Stimac, J., Sihotang, A.M., Mussofan, W., et al., 2019. Geologic controls on the Muara Laboh geothermal system, Sumatra, Indonesia. Geothermics 82. https://doi.org/10.1016/j.geothermics.2019.06.002. Volume.
Sruoga, P., Rubinstein, N., 2007. Processes controlling porosity and permeability in volcanic reservoirs from the Austral and Neuquén basins, Argentina. AAPG Bull. 91, 115–129. https://doi.org/10.1306/08290605173.
Vidal, J., Genter, A., Chopin, F., 2017. Permeable fracture zones in the hard rocks of the geothermal reservoir at Rittershoffen, France. J. Geophys. Res. Solid Earth 122, 4864–4887. https://doi.org/10.1002/2017JB014331.
Voutilainen, M., Miettinen, A., Sardini, P., et al., 2019. Characterization of spatial porosity and mineral distribution of crystalline rock using X-ray micro computed tomography, C-14-PMMA autoradiography and scanning electron microscopy. Appl. Geochem. 101, 50–61. https://doi.org/10.1016/j.apgeochem.2018.12.024. VolumePages.
Vuollo, J., Huhma, H., Lehtinen, M., Nurmi, P.A., Rämö, O.T., 2005. Paleoproterozoic mafic dikes in NE Finland. Precambrian Geology of Finland: Key to the Evolution of the Fennoscandian Shield. Developments in Precambrian Geology 14. Elsevier, pp. 195–236. Amsterdam.
Weydt, L.M., Lucci, F., Lacinska, A., et al., 2022. The impact of hydrothermal alteration on the physiochemical characteristics of reservoir rocks: the case of the Los Humeros geothermal field (Mexico). Geotherm. Energy 10, 20. https://doi.org/10.1186/s40517-022-00231-5.
Wyering, L.D., Villeneuve, M.C., Wallis, I.C., Siratovich, P.A., Kennedy, B.M., Gravley, D. M., Cant, J.L., 2014. Mechanical and physical properties of hydrothermally altered rocks, Taupo Volcanic Zone, New Zealand. J. Volcanol. Geotherm. Res. 288, 76–93. https://doi.org/10.1016/j.jvolgeores.2014.10.008.
Zangerl, C., Evans, K.F., Eberhardt, E., Loew, S., 2008. Normal stiffness of fractures in granitic rock: a compilation of laboratory and *in-situ* experiments. Int. J. Rock Mech. Min. Sci. 45 (8), 1500–1507. https://doi.org/10.1016/j.ijrmms.2008.02.001. VolumeIssuePages.